

1 **Surface Shortwave Aerosol Radiative Effect During the ARM Mobile**  
2 **Facility Deployment in Niamey, Niger**

3  
4 S.A. McFarlane, E.I. Kassianov, J. Barnard, C. Flynn  
5 Atmospheric Science and Global Change Division, Pacific Northwest National  
6 Laboratory, Richland, WA

7  
8 T. P. Ackerman  
9 Joint Institute for the Study of the Atmosphere and Oceans and Department of  
10 Atmospheric Sciences, University of Washington, Seattle, WA

11  
12 Submitted to J. Geophys. Res., May 26, 2008

13  
14 \*Corresponding author: Sally McFarlane, Pacific Northwest National Laboratory, P.O.  
15 Box 999, MSIN K9-24, Richland, WA, 99352. Tel. (509) 375-6402; Fax (509) 375-6448

16  
17

18 Abstract

19

20 Ground-based remote sensing measurements of aerosol optical properties and  
21 corresponding shortwave surface radiative effect calculations for the deployment of the  
22 Atmospheric Radiation Measurement (ARM) Program's Mobile Facility (AMF) to  
23 Niamey, Niger during 2006 are presented. Aerosol optical properties including aerosol  
24 optical depth (AOD), single scattering albedo (SSA), and asymmetry parameter (AP)  
25 were derived from multi-filter rotating shadowband radiometer (MFRSR) measurements  
26 during two dry seasons (Jan-Apr and Oct-Dec) at Niamey. The vertical distribution of  
27 aerosol extinction was derived from the collocated micropulse lidar. The aerosol optical  
28 properties and vertical distribution varied significantly throughout the year, with higher  
29 AOD, lower SSA, and deeper aerosol layers during the Jan-Apr time period.

30

31 Using the retrieved aerosol properties, broadband shortwave surface fluxes and  
32 atmospheric heating rate profiles were calculated. Corresponding calculations with no  
33 aerosol were used to estimate the aerosol direct radiative effect at the surface.  
34 Comparison of the calculated surface fluxes to observed fluxes for non-cloudy periods  
35 indicated that the remote sensing retrievals provided a reasonable estimation of the  
36 optical properties, with mean differences between calculated and observed fluxes of less  
37 than  $5 \text{ W/m}^2$  and RMS differences less than  $25 \text{ W/m}^2$ . Sensitivity tests for a case study  
38 showed that the observed fluxes could be matched with variations of  $< 10\%$  in the inputs  
39 to the radiative transfer model. The average daily SW aerosol radiative effect over the  
40 study period was estimated to be  $-27 \text{ W/m}^2$ , which is comparable to values estimated  
41 from satellite data and from climate models with sophisticated dust parameterizations.

42

## 43 **1.0 Introduction**

44

45 Understanding the impact of anthropogenic aerosol radiative forcing is important in  
46 predicting future climate change. It is difficult to accurately model aerosol radiative  
47 forcing in global climate models because the radiative forcing of aerosol varies  
48 considerably with the composition and optical properties of the aerosol, and is therefore  
49 strongly regionally dependent. Recent studies have indicated the importance of mineral  
50 dust aerosol to climate, due both to direct radiative forcing (Haywood et al., 2003;  
51 Haywood et al. 2005; Highwood et al. 2003) and to potential influences on tropical  
52 cyclogenesis (Dunion and Velden 2004). The Sahara is an important source region for  
53 mineral dust aerosol; mineral dust plumes originating in Africa frequently travel over the  
54 Atlantic Ocean, some reaching as far as the eastern United States (Prospero and Lamb  
55 2003). Anthropogenic factors, such as over-grazing in the Sahel region (the southern  
56 border of the Sahara), may lead to changes in the amount of mineral dust aerosol, making  
57 it an important factor to consider in estimates of anthropogenic climate change (Tegen et  
58 al.1996, Mahowald et al. 2004).

59

60 Estimates of the effect of mineral dust on the top of atmosphere (TOA) radiation budget  
61 have been made using satellite (Li et al. 2004) and aircraft observations (Haywood et al.  
62 2003; Highwood et al. 2003), but limited observations of aerosol radiative effects in the  
63 Sahel have been made at the surface. In 2006, the Atmospheric Radiation Measurement  
64 (ARM) program's Mobile Facility (AMF) was deployed to Niamey, Niger for the year-  
65 long Radiative Atmospheric Divergence Using the AMF, GERB Data, and AMMA  
66 Stations (RADAGAST) experiment (Miller and Slingo, 2007). This deployment of the  
67 AMF, which is a mobile suite of ground-based remote sensing instruments similar to  
68 those found at a fixed ARM site, provides the first extended time series of aerosol and  
69 collocated broadband radiation measurements at the ground in the Sahel region.

70

71 The combination of the AMF measurements with the Geostationary Earth Radiation  
72 Budget (GERB; Harries et al. 2005) broadband radiometer and the multi-channel

73 Spinning Enhanced Visible and Infrared Imager (SEVIRI; Schmetz et al. 2002) onboard  
74 the *Meteosat-8* geostationary satellite will allow examination of the radiative divergence  
75 of the atmospheric column. Climate models may be tuned to produce agreement with  
76 observed globally averaged radiative fluxes at the top of the atmosphere (TOA) from  
77 satellite measurements, but they often have trouble matching both the TOA and surface  
78 radiation budgets simultaneously (Wild et al., 2006). Combining the surface and satellite  
79 measurements to estimate the radiation budget of the entire column will provide an  
80 important constraint for climate model evaluation. As a first step, both the surface and  
81 TOA measurements need to be evaluated independently. In this study, we focus on  
82 examining the aerosol properties and surface radiative effects measured by the AMF.

83

84 Slingo et al. (2008) provide an overview of the meteorological and thermodynamic  
85 conditions observed at Niamey during the RADAGAST experiment. Niamey has a  
86 monsoonal climate with a high rainfall period occurring in May through September and  
87 very little rainfall at other times of the year. During the AMF deployment, the onset of  
88 the wet season, which is marked by the northward passage of the Inter-Tropical Front  
89 (ITF) through Niamey, occurred on May 5, 2006. The end of the wet season, which is  
90 marked by a sudden drop in dew point temperature as the ITF passes southward through  
91 Niamey, occurred later than usual, near the end of October (Slingo et al. 2008).

92 However, although there was increased moisture in the atmosphere associated with the  
93 monsoon season, no precipitation was recorded at the AMF site during the month of  
94 October. During the wet season, clouds dominate the radiative forcing at both the surface  
95 and TOA, but during the dry season the effects of dust and biomass burning aerosol  
96 dominate the surface radiative forcing (Slingo et al. 2008b).

97

98 In this study, we focus on quantifying the shortwave aerosol radiative effect at the surface  
99 during the dry season, from Jan 9 – April 31 and Oct 6 – Dec 31, 2006. We assess our  
100 ability to reproduce the measured shortwave radiative fluxes at the surface for the range  
101 of aerosol conditions observed during the period using aerosol optical properties  
102 measured by the AMF and a state of the art radiative transfer model. This type of  
103 radiative closure study is important to identify possible shortcomings in aerosol property

104 retrieval algorithms or the treatment of aerosol in current radiative transfer models  
105 (Michalsky et al. 2006). Additionally, we present initial estimates of the vertical profile  
106 of shortwave radiative heating in the atmospheric column over Niamey.

## 107 **2.0 Data and Methodology**

108 The deployment of the AMF to Niamey is described in detail in Miller and Slingo (2007).  
109 In this section we describe only the particular instruments and retrievals used in our  
110 study. The AMF was deployed at the Niamey airport (13.48° N, 2.18° E) from January  
111 through December, 2006 with the official start of operations occurring 9 Jan 2006. An  
112 ancillary site, containing only radiation and surface meteorological instruments was  
113 deployed at Banizoumbou, Niger (13.52° N, 2.63° E). Data from the AMF instruments  
114 are freely available from the ARM archive ([www.archive.arm.gov](http://www.archive.arm.gov)).  
115

116 The AMF deployment to Niamey was timed to coincide with the special observing  
117 periods of the African Multidisciplinary Monsoon Analysis (AMMA; Redelsperger et al.  
118 2006), an extensive project to study the West African monsoon. Measurements taken as  
119 part of AMMA are useful for placing the AMF observations in context. In particular, in  
120 situ measurements taken during aircraft flights out of Niamey in January 2006 as part of  
121 the Dust and Biomass Experiment (DABEX; Johnson et al. 2008a, Johnson et al. 2008b,  
122 Osborne et al. 2008) provide information about the vertical structure of the aerosol  
123 composition over Niamey.

### 124 **2.1. Meteorological Measurements**

125 Vertical profiles of atmospheric temperature and water vapor at 15-minute resolution are  
126 calculated following the method of Mather et al. (2007) in which vertical profile  
127 information from radiosondes (which are launched 4 times/day at AMF site) are  
128 combined with more frequent measurements of precipitable water vapor (PWV) from a 2-  
129 channel microwave radiometer (MWR) and surface air temperature (from a surface  
130 meteorological station). Above 20 km, radiosonde profiles are not valid and information  
131 from a standard atmospheric profile is used. The surface skin temperature is obtained  
132 from a downward looking infrared thermometer (IRT).

## 133 **2.2. Broadband Radiation Measurements**

134 Downwelling shortwave (SW) broadband radiation measurements at 1-minute resolution  
135 were provided by a suite of radiometers. Diffuse broadband SW radiation was measured  
136 by an Eppley Model 8-48 black and white pyranometers and direct SW radiation by a  
137 normal incidence pyrliometer (NIP). Total SW downwelling flux is calculated using  
138 the component sum method, which consists of combining the measured diffuse irradiance  
139 and the direct normal irradiance from the NIP multiplied by the cosine of the solar zenith  
140 angle. Upwelling broadband SW irradiance was measured by a downward looking  
141 pyranometer, mounted at approximately 2 m above the surface. The ratio of the  
142 upwelling to downwelling flux is used to estimate the local broadband albedo at the site.

143

144 The radiometers at the AMF were cleaned daily. The best estimates of the accuracy of  
145 the downwelling radiation measurements from years of operation during the ARM  
146 program are  $13.6 \text{ Wm}^{-2}$  (direct),  $9.0 \text{ Wm}^{-2}$  (diffuse) and  $9.0 \text{ Wm}^{-2}$  (total), as reported in  
147 Slingo et al. (2006). Uncertainties are likely to be larger during unusual circumstances,  
148 such as very high turbidity during dust storms.

149

150 Detailed spectral information about the surface albedo at Niamey is required for the  
151 aerosol optical property retrievals (section 4) and the radiative transfer calculations  
152 (section 5). However, this information is not available. We use a spectral albedo of dry  
153 sand (Tanre et al. 1986) and scale the profile so that the broadband albedo matches the  
154 daily average broadband albedo that is calculated from the ratio of the average upwelling  
155 and downwelling fluxes measured by the pyranometers between 10:00 and 16:00 LST  
156 each day. During the AMF deployment, a white cooling box was located within the field  
157 of view of the downward-looking pyranometers. The effect of this bright white surface  
158 within the field of view is expected to increase the broadband albedo by several percent  
159 over the actual value. The broadband surface albedo at Niamey (Fig 1) varies over the  
160 deployment period from an average of 0.25 during the first observed dry season (Jan –  
161 Apr) to 0.20 during the wet season (May-Sept) and 0.23 during the second observed dry  
162 season (Oct - Dec) as the surface vegetation and soil moisture change. The peak in  
163 albedo at day 66 corresponds to the March dust storm and may be due to dust on the

164 radiometers. The noise in the albedo during the wet season is likely due to the impact of  
165 precipitation on the surface albedo – wet and dry soils can have significantly different  
166 SW albedos (Idso et al 1975).

167

168 Examination of satellite surface albedo retrievals indicates that the region around Niamey  
169 has a very heterogeneous surface albedo and the local-scale albedo derived from the  
170 upward- and downward-looking pyranometers may not be representative of the larger  
171 area (Settle et al. 2008). The local broadband albedo at the Banizoumbou site, which is  
172 more vegetated than the Niamey site, shows the same temporal variation as the Niamey  
173 site during the first part of the year, but is generally 0.05 higher (Fig 1). During the 2<sup>nd</sup>  
174 dry season, the Banizoumbou albedo increases more rapidly than the Niamey site,  
175 perhaps due to the differing surface properties at Banizoumbou.

### 176 **2.3. Aerosol Remote Sensing Measurements**

177 Column-integrated values of aerosol optical depth (AOD), Angstrom exponent, and  
178 aerosol optical properties are calculated from the Multi-Filter Rotating Shadowband  
179 Radiometer (MFRSR) data at the Niamey and Banizoumbou sites. The MFRSR measures  
180 total and diffuse solar irradiance at six wavelengths (415, 500, 615, 673, 870, 940 nm).  
181 Direct solar irradiance is obtained by differencing the total and diffuse measurements,  
182 and spectral values of aerosol optical depth are obtained via a Langley regression  
183 (Harrison and Michalsky, 1994). The Angstrom exponent is calculated from the optical  
184 depths at 415 and 870 nm. For a well-calibrated MFRSR, uncertainty in retrieved AOD  
185 is estimated to be 0.01 (Michalsky et al. 2001, Alexandrov et al. 2007). A detailed  
186 examination of possible sources of error in MFRSR AOD retrievals can be found in  
187 Alexandrov et al. (2007). The MFRSR uses a shadow-band to block the sun for the  
188 diffuse sky measurement, and estimates the solar aureole contribution to the blocked  
189 measurement by taking two sideband measurements. For most aerosol conditions, errors  
190 in AOD due to the underestimate of the solar aureole contribution are negligible, however  
191 they become more significant for aerosol effective radius  $> 1 \mu\text{m}$  due to the larger  
192 forward scattering contributions (Alexandrov et al. 2007).

193

194 Column-averaged values of aerosol single scattering albedo (SSA) and asymmetry  
195 parameter (AP) at MFRSR wavelengths below 940 nm are retrieved from MFRSR  
196 observations using the retrieval technique described in Kassianov et al. (2007). In this  
197 retrieval, the aerosol size distribution is assumed to be well modeled by a bimodal  
198 lognormal distribution of spherical particles. The widths (variance) of the fine and coarse  
199 modes and real part of the refractive index are assumed known. The retrieval is  
200 performed in two steps. First, the parameters of the two lognormal distributions (volume  
201 median particle radius and volume concentration of each mode) are iterated to match the  
202 observed spectral dependence of the AOD. Since the contribution of the coarse mode to  
203 the spectral variability of AOD in the MFRSR spectral range (415-870 nm) is relatively  
204 small, the retrieval is not sensitive to the coarse mode. Second, the value of the imaginary  
205 refractive index is iterated until the calculated spectral values of the ratio of the diffuse to  
206 direct irradiances matches the observed values. The second step involves an additional  
207 assumption that the spectral values of surface albedo (at MFRSR wavelengths) are  
208 known. Kassianov et al. (2006) illustrated that uncertainties in the surface albedo only  
209 weakly affect the MFRSR-retrieved SSA and AP values when the surface albedo is  
210 relatively small ( $\sim 0.1$ ). For Niamey, such small values are observed for two wavelengths  
211 (415 and 500 nm). As a result, we expect that surface albedo variations do not  
212 substantially change the MFRSR-retrieved SSA and AP values for these two  
213 wavelengths. Uncertainties in MFRSR-retrieved SSA and AP values associated with  
214 uncertainties in AOD values and size distribution assumptions vary, on average, in 0.03-  
215 0.04 range for typical values of AOD (0.1-0.3 at 500 nm) (Kassianov et al., 2007).  
216 However, these uncertainties can be substantially larger for cases with large aerosol  
217 loading (e.g., during dust storms).

218

219 An additional factor which can contribute to uncertainties in MFRSR-retrieved optical  
220 properties of aerosol is nonsphericity of aerosol particles. Since dust particles have  
221 complex geometrical shapes (e.g., Kalashnikova and Sokolik 2004), the influence of  
222 particle nonsphericity on aerosol optical properties has been addressed by numerous  
223 studies (e.g., Yang et al., 2007 and references therein). In particular, the modeling results  
224 demonstrated that particle nonsphericity can substantially change the scattering phase

225 function, but has little impact on the total optical cross section, SSA and AP (e.g.,  
226 Mishchenko et al.1997, Yang et al. 2007). As a result, the influence of particle shape is  
227 important in aerosol retrievals based on multiangular satellite (Kahn et al. 1997) or  
228 ground-based observations (Dubovik et al. 2006). The MFRSR retrieval discussed here  
229 involves diffuse irradiance from hemispherical observations. This irradiance is a function  
230 of the AOD, SSA and AP, and therefore it should not be very sensitive to details of  
231 scattering phase function associated with the particle shapes. The same should be true for  
232 the MFRSR-derived aerosol optical properties. However, accounting for the effects of  
233 nonspherical aerosol particles in the MFRSR retrieval and estimation of associated  
234 uncertainties in retrieved optical properties requires further investigation.

235

236 AOD and Angstrom exponent retrievals are performed between 0800 and 1800 LST at  
237 20-second resolution for the entire deployment. The aerosol optical properties (SSA and  
238 AP) are retrieved only during the dry periods (Jan-Apr and Oct-Dec) for times between  
239 1000 and 1600 LST at 1-minute resolution. We apply a cloud-screening methodology  
240 based on the variability of the retrieved AOD and remove all AOD and optical property  
241 retrievals for times identified as cloudy. We interpolate the AOD and optical property  
242 measurements over cloudy periods and missing (including nighttime) data to develop a  
243 continuous time series.

244

245 Information on aerosol optical properties in the longwave spectrum can be retrieved from  
246 the Atmospheric Emitted Radiance Interferometer, which was also deployed in Niamey  
247 as part of the AMF (Turner 2008). In this study we focus only the shortwave optical  
248 properties and radiative effects at the surface. In future work we plan to combine the  
249 shortwave and longwave measurements to get a consistent picture of the aerosol  
250 properties and radiative effects.

#### 251 **2.4. Aerosol Extinction Profiles**

252 Vertical profiles of aerosol extinction were calculated using a micropulse lidar (MPL)  
253 and the column AOD retrieved from the MFRSR. The MPL is a 523-nm eye-safe  
254 autonomous lidar system (Campbell et al., 2002). The measured backscatter profile is

255 corrected for dead-time, after-pulse, background signal and overlap using standard  
256 methods (Campbell et al. 2002). Large changes in temperature can affect the operation of  
257 the MPL by leading to changes in the telescope focus which affect the overlap correction  
258 (E.J. Welton, personal communication, 2006). Due to the environmental conditions  
259 expected at Niamey (where the diurnal change in temperature can be as large as 19K),  
260 additional temperature control measures were added to the MPL container as part of the  
261 AMF deployment. During the Niamey deployment, the mean diurnal variation in laser  
262 temperature was  $< 3\text{K}$ , which should not result in significant variations in the overlap  
263 correction.

264

265 Vertical profiles of aerosol extinction are retrieved from the lidar backscatter  
266 measurements following the method of Welton et al. (2000). MPL backscatter profiles  
267 are averaged over 15 minutes to improve the signal to noise ratio. A cloud detection  
268 algorithm based on the method of Pal et al. (1992) is implemented to identify clouds in  
269 the MPL data. For the non-cloudy daytime periods, the value of the extinction-  
270 backscatter ratio (also known as the lidar ratio,  $S$ ) is iterated in the lidar inversion  
271 equation (Fernald 1984) until the AOD calculated from the lidar extinction profile  
272 matches the AOD value derived from the MFRSR measurements. The retrieved lidar  
273 ratio is interpolated across nighttime and cloudy periods.

274

275 Visual inspection of the MPL images and aircraft profiles over Niamey from DABEX in  
276 January 2006 indicate that the aerosol observed at Niamey is generally confined to the  
277 lowest 7 km of the atmosphere. For nighttime periods or time periods where the MPL  
278 detects cirrus cloud above 8 km and there are no AOD retrievals, we calculate the  
279 extinction profile by using the interpolated lidar ratio in the Fernald (1984) forward  
280 equation. For times where the MPL detects cloud below 8 km, the MPL profile at this  
281 time is not used, and the extinction is interpolated in time. The MPL shutter is closed for  
282 a half-hour period near local solar noon each day to protect the optics from the nearly-  
283 overhead sun. The calculated extinction profile is interpolated over these periods.

284

## 285 **2.5. Radiative Transfer Calculations**

286 We calculate shortwave broadband fluxes and radiative heating rate profiles at the AMF  
287 site in Niamey using the 1D version of the SHDOM radiative transfer model (Evans,  
288 1998) combined with the RRTM correlated k-distribution (Clough et al. 2005; McFarlane  
289 and Evans 2004). To best match the characteristics of the Eppley radiometers, we use 13  
290 bands in the shortwave, from 0.2 – 3.86  $\mu\text{m}$ . This set of radiative transfer models was  
291 chosen because of its high accuracy and the flexibility of the input parameters; the  
292 extinction, single-scattering albedo, and Legendre coefficients of the scattering phase  
293 function are specified for each wavelength band at each input grid-point. For this study,  
294 we assume the aerosol phase function can be modeled by a Henyey-Greenstein phase  
295 function.

296

297 Aerosol optical properties must be extrapolated from the 5 MFRSR wavelengths to the 14  
298 wavelength bands used in the radiative transfer model. The AOD is extrapolated using

299 the Angstrom expression  $\tau_\lambda = AOD_0 \left( \frac{\lambda}{\lambda_0} \right)^{-\alpha}$  where  $\lambda$  is the desired wavelength,  $\lambda_0$  is

300 415 nm,  $AOD_0$  is the AOD at 415 nm, and  $\alpha$  is the Angstrom exponent. Use of the  
301 Angstrom expression to extrapolate AOD beyond measured wavelengths has been shown  
302 to give the best fit to observed fluxes (Michalsky et al. 2006). The extrapolation of single  
303 scattering albedo and asymmetry parameter is less well-constrained since the ultraviolet  
304 (UV) and near-infrared (IR) aerosol properties are not known. We extrapolate the single  
305 scattering albedo (SSA) and asymmetry parameters (AP) to the center wavelengths of the  
306 radiative transfer model bands using exponential fits based on the observed wavelength  
307 dependence. For the SSA, the exponential increases with increasing wavelength;  
308 however the SSA at wavelengths greater than 870 nm is fixed to the MFRSR derived  
309 value at 870 nm. For the AP, the exponential fit decreases with increasing wavelength.  
310 For cloudy periods, the aerosol properties obtained during adjacent clear-sky periods are  
311 interpolated. The vertical distribution of the aerosol is determined by the extinction  
312 profile calculated from the MPL as described above.

313

314 We perform radiative transfer calculations at 15-minute resolution for the periods Jan –  
315 April and Oct-Dec, 2006 at the Niamey airport site. Two sets of calculations are  
316 performed using the same set of temperature and humidity profiles; one with aerosol  
317 (AER) and one without aerosol (CLEAR). No clouds are included in the radiative  
318 transfer calculations. A sensitivity analysis of the radiative transfer calculations is  
319 performed in Section 4.2.

320

## 321 **3.0 Aerosol Results**

### 322 **3.1. *Aerosol Optical Properties***

323 In this section, we examine the statistics of the time series of aerosol measurements and  
324 compare the aerosol properties to those reported in the literature. The time series of  
325 daily-averaged, cloud-screened AOD (Figure 2) indicates the large variability in aerosol  
326 optical depths seen in Niamey, with daily-averaged AOD at 500 nm ranging from a low  
327 of 0.08 during November to a high of 2.5 during the peak of a dust storm which occurred  
328 in March (Slingo et al. 2006). Peaks in AOD throughout the year, including the broad  
329 peak in June, are associated primarily with other dust transport events. Although the data  
330 at the Banizoumbou site is more limited, the good correspondence between the time  
331 series of retrieved AOD at the two sites, which are located roughly 60 km apart, indicates  
332 that much of the daily aerosol variability is controlled by large-scale rather than local  
333 influences.

334

335 Large variability in the retrieved Angstrom exponent and column-integrated aerosol  
336 optical properties is seen throughout the year (Figure 3; Table 1), which is likely due to  
337 variability in the relative amounts of dust and biomass burning aerosol in the column.  
338 Biomass burning in Africa occurs on a seasonal cycle, related to changes in precipitation.  
339 Satellite observations of fire counts and smoke-related aerosols indicate that burning in  
340 the Sahel region generally begins in October-November, peaks in January, and then  
341 declines throughout the spring, with little biomass burning observed in May through  
342 September (Duncan et al. 2002). Aircraft flights out of the Niamey airport during the

343 DABEX experiment indicated the frequent occurrence of biomass burning aerosol layers  
344 existing above dust layers (Johnson et al. 2008a, Osborne et al. 2008). Back-trajectory  
345 analysis (Slingo et al. 2008a) indicated that air parcels observed at 500 m and 1000 m  
346 over Niamey during the dry season were primarily from the north and east. Many of  
347 these trajectories passed over the Bodele depression in Chad, a major dust source region.  
348 During Jan-Apr, a large percentage of the air parcels at 4000 m originated from south and  
349 east of Niamey (i.e., over Nigeria, a source of biomass burning aerosol) while the  
350 trajectories were more variable during Oct-Dec. During the Jan-Apr part of our study  
351 period, when biomass burning was more prevalent near Niamey, the Angstrom exponent  
352 is much higher (indicating smaller particles), the SSA is lower (indicating more  
353 absorbing aerosol) (Table 1). The SSA and AP show larger variability with wavelength in  
354 Jan-Apr time period than in the Oct-Dec period (Table 2). Note, this variability represents  
355 observations with 1-minute resolution. Corresponding daily-averaged variability is  
356 smaller (Figure 3).

357

358 Estimates of optical properties of mineral dust in the literature show a wide range of  
359 values. Previous studies have indicated that optical properties of mineral dust are  
360 strongly tied to the mineral composition of the dust and may vary significantly with dust  
361 source region (Sokolik and Toon 1999, Koven and Fung, 2006). The red color of the dust  
362 from visual observations and the strong absorption in the MFRSR blue wavelength (415  
363 nm) relative to the other wavelengths indicates that the dust at Niamey probably contains  
364 iron oxides, such as hematite. Alfaro et al. (2004) performed laboratory studies to  
365 examine the absorption of desert dust aerosols as a function of iron oxide content. They  
366 found that mass absorption efficiencies at 325 nm were approximately 6 times larger than  
367 those at 660 nm for samples containing iron oxide and that absorption efficiency  
368 increased linearly with iron oxide content. Their soil sample from Niger had the largest  
369 iron oxide content (6.5% by mass) of the three desert samples studies. Turner (2008)  
370 retrieved dust mineral composition from AERI measurements during the AMF  
371 deployment by using the differences in longwave absorption features of several minerals  
372 to distinguish between them. However, iron oxides have no spectral absorption features  
373 in the 8-13 um band so cannot be identified by the AERI measurements. Turner (2008)

374 found that gypsum and kaolinite were the most common components contributing to the  
375 LW absorption and that the mineral composition of the dust varied with both the stage of  
376 the monsoon and the prevailing wind direction.

377

378 Carlson and Benajmin (1980) performed an early study of radiative heating of Saharan  
379 dust and summarized available measurements of dust refractive indices. They show an  
380 order of magnitude range of variability in the imaginary component of the refractive  
381 index (which is related to absorption), especially in the 500-700 nm region (their Fig 3).  
382 Similarly, Sokolik and Toon (1996) reported visible SSA values from the literature  
383 ranging from 0.6 – 0.95 and asymmetry values from 0.65 to 0.94. Fouquart et al. (1987)  
384 derived SSA of dust from in situ broadband radiation measurements near Niamey in Oct-  
385 Dec 1980. They found a mean SSA of 0.95, with a range from 0.93-0.99. More recent  
386 studies of Saharan dust have reported values in general agreement with the values found  
387 by Fouquart et al. (1987). Kaufman et al. (2001) derived a SSA of 0.97 at 0.64  $\mu\text{m}$  from  
388 satellite measurements of Saharan dust over Senegal although slightly smaller SSA  
389 (around 0.92) were found from ground-based remote sensing measurements. During the  
390 Saharan Dust Experiment (SHADE), which examined aerosol advected off the coast of  
391 West Africa, Haywood et al. (2003) measured values of SSA at 550 nm ranging from  
392 0.95 to 0.99 with in situ aircraft instruments. These more recent studies suggest that  
393 lower values of SSA found for mineral dust in previous experiments were due to mixing  
394 of mineral dust with more absorbing aerosol, such as that produced by biomass burning  
395 or pollution.

396

397 The range of SSA retrieved from the MFRSR at 500 nm during the Jan-Apr period is  
398 0.73 to 1.00 (Table 2), which is consistent with the range of values reported in the  
399 literature and is also consistent with values of SSA measured by the aircraft instruments  
400 during DABEX (Johnson et al. 2008a; Osborne et al. 2008). Osborne et al. 2008  
401 reported SSA (at 550 nm) as a function of height from all level aircraft runs within the  
402 vicinity of Niamey or Banizoumbou (their Fig 10. Values of SSA measured by the in situ  
403 aircraft range from  $\sim$ 0.70 to 1.00 and show a dependence on height, with lower SSA  
404 values ( $<$  0.8) associated with biomass burning aerosol or mixed aerosol conditions above

405 2000 m, intermediate values of SSA between 1000-2000 m, and higher SSA values (>  
406 0.96) associated with dust below 1000 m. During a flight northeast of Niamey, the  
407 aircraft also sampled a ‘pure’ dust layer, which had SSA of 0.99.

408

409 Since the MFRSR retrieves column-integrated values, we can not separate out the  
410 contributions of dust and biomass burning aerosol to the retrieved optical properties.  
411 During the second observed dry period, when less biomass burning aerosol is expected  
412 near Niamey, the average SSA and AP retrieved from the MFRSR are higher than in the  
413 Jan-Apr period. However, there is still a relatively large range in SSA at 500 nm (from  
414 0.82 to 1.00), which does not agree with the DABEX low-altitude dust measurements.  
415 This range in retrieved optical properties from the MFRSR may indicate differences in  
416 mineral composition of the dust or the influence of local industrial or cookfire emissions  
417 from the Niamey area on the AMF measurements.

418

### 419 **3.2. Aerosol Vertical Profiles**

420 The MFRSR only measures column-integrated aerosol properties. However, information  
421 on the vertical distribution of aerosol throughout the AMF deployment is available from  
422 the MPL. These measurements, along with the other lidar deployments during AMMA  
423 (e.g. Heese et al. 2008), represent the first set of ground-based lidar measurements in the  
424 Sahel region. The MPL derived extinction profiles (described in Section 2.4) were  
425 compared to observations from the in situ aircraft probes for profiles taken with 100 km  
426 of the Niamey airport during Jan-Feb 2006 (Johnson et al. 2008b). In these comparisons,  
427 the MPL and aircraft extinction profiles generally compared well in the upper layers  
428 (above 2000 m) while the aircraft overestimated the extinction relative to the MPL in the  
429 layers dominated by dust aerosol. This disagreement may be partly caused by the  
430 assumption of a constant lidar ratio in the MPL retrieval algorithm, which may cause the  
431 MPL to overestimate the extinction due to biomass burning aerosol (which has a lower  
432 lidar ratio than dust) and underestimate the extinction due to dust layers. There is also  
433 uncertainty in the aircraft profiles, due to correction factors required for the in situ  
434 aircraft probes. Comparisons of the aircraft AOD to AERONET retrievals at

435 Banizoumbou indicate that the aircraft overestimates AOD by 10-20% for columns  
436 dominated by biomass burning aerosol extinction and overestimates by 30-40% for  
437 columns dominated by dust aerosol extinction (Johnson et al. 2008b).

438

439 To estimate the uncertainty in the MPL extinction profiles associated with the assumption  
440 of a constant lidar ratio, a simple sensitivity test was performed. An idealized aerosol  
441 extinction profile was constructed, consisting of a dust aerosol from 0-2 km and biomass  
442 burning aerosol from 2-6 km. The total AOD of the profile was 0.61, with dust aerosol  
443 contributing 72% of the extinction and biomass burning aerosol contributing 28% of the  
444 extinction. These values are based on the DABEX campaign-averaged profile (Johnson  
445 et al. 2008b). Given the idealized aerosol extinction profile, a standard molecular  
446 scattering profile, and the average backscatter-extinction ratios for dust (55 Sr) and  
447 biomass burning aerosol (75 Sr) calculated by Heese et al. (2008) from Raman lidar  
448 measurements during the DABEX campaign, a theoretical backscattering profile was  
449 calculated. This profile was input to the lidar inversion algorithm and the extinction  
450 profile was retrieved assuming a constant lidar ratio. The resulting retrieved column lidar  
451 ratio was 58.8 Sr, close to the assumed value of 55 Sr for the dust aerosol layer, due to  
452 the fact that the dust aerosol dominated the total extinction. At the peak of the dust layer  
453 (extinction values of  $0.58 \text{ km}^{-1}$ ) the extinction was overestimated by 6%; while at the  
454 peak of the biomass burning aerosol layer (extinction values of  $0.09 \text{ km}^{-1}$ ) the  
455 extinction was underestimated by 18%. This sensitivity test illustrates that the vertical  
456 extinction is sensitive to the use of a constant lidar ratio, but the uncertainty is larger for  
457 the biomass burning layer since the dust tends to dominate the extinction in the column.

458

459 Additional uncertainty in the MPL profiles, especially close to the surface, may be caused  
460 by uncertainty in the lidar overlap correction. The overlap function is a multiplicative  
461 factor that corrects for loss of signal due to poor optical efficiency of the telescope in the  
462 near-range of the lidar. For the Niamey MPL, the overlap correction is significant ( $> 3\%$ )  
463 to a distance of about 3.5 km. The exact uncertainty in the overlap function used for the  
464 Niamey MPL is not available; error analysis by Welton and Campbell (2002) indicates

465 that uncertainty in the overlap correction is typically on the order of 5-10% of the overlap  
466 function itself.

467

468 A curtain-plot of cloud-screened MPL-derived aerosol extinction during the dry season is  
469 shown in Figure 4. During the first observed dry period there is significantly more  
470 variability above 2 km, which is associated with the frequent presence of biomass  
471 burning aerosol layers. The few points with very high aerosol extinction above 4 km are  
472 likely thin clouds that were not caught by the cloud-screening algorithm. The  
473 background AOD level is higher in the Jan-Apr period than in the Oct-Dec period,  
474 although both periods show frequent spikes in AOD associated with dust events. The  
475 MPL extinction profiles show clear seasonal differences in the vertical distribution of  
476 aerosol (Fig 5). Large dust storms occurred in both dry periods, giving Mar, April, and  
477 Dec the largest average extinction values. During the early dry period, the extinction  
478 profiles peak near 500 m in all months while in the later period the aerosol extinction  
479 profiles peak much closer to the surface, near 100 m. Analysis of the radiosondes from  
480 the AMF (Slingo et al. 2008a; Figure 11) indicates that the mixed layer is often deeper in  
481 the beginning of the year which may result in the aerosol mixing higher in the boundary  
482 layer.

483

484 Over land, close to the aerosol source regions, dust is generally found in the boundary  
485 layer. However, as Saharan dust is transported off the coast of West Africa by the  
486 easterly winds, it is generally elevated as the dry, dusty air layer is undercut by cool,  
487 moist maritime air (Prospero and Carlson 1981). Thus vertical profiles of the dust off  
488 the coast of W. Africa are often quite different from those over land, closer to the dust  
489 source regions.

490

## 491 **4.0 Aerosol Direct Radiative Effect**

### 492 **4.1. Case Study**

493 To illustrate the effects of aerosol at Niamey on the SW surface fluxes and heating rates,  
494 we examine the results for a case study on Jan 21, 2006. During the dry season at  
495 Niamey, the typical atmospheric structure consisted of multiple atmospheric layers in the  
496 mid-troposphere, often with large humidity differences between layers (Slingo et al.  
497 2008a). The strong solar heating near the surface often created a deep, well-mixed layer  
498 during the daytime. The Jan 21 case exemplifies this structure. Aircraft profiles during  
499 the DABEX experiment indicated that the total aerosol extinction in the atmospheric  
500 column over Niamey on Jan 21 was dominated by dust aerosol although biomass burning  
501 aerosol existed above 2 km (Ben Johnson, personal communication 2007). The corrected  
502 backscatter and extinction profiles derived from the MPL for the daylight hours of Jan 21  
503 show that the majority of the aerosol loading and extinction is below 1 km, although  
504 significant amounts of aerosol exist up to 5km (Figure 6). Considerable vertical structure  
505 is seen in the aerosol layers throughout the day. The aerosol optical properties were  
506 fairly constant over the day. The AOD at 500 nm ranged from 0.45 to 0.53 between 06:30  
507 and 17:15 UTC. The average values of the single-scattering albedo and asymmetry  
508 parameter at 500 nm were 0.89 and 0.68, respectively, and both of these parameters had  
509 standard deviations less than 0.01 over the daylight period.

510

511 Good agreement is seen between the observed (OBS) fluxes and the calculated AER  
512 fluxes for this case study (Figure 7 and Table 3). Average differences, given as AER-  
513 OBS for the 06:30-17:15 UTC period are  $4.1 \text{ Wm}^{-2}$  for the direct flux (1.4% of the  
514 average observed flux),  $11.6 \text{ Wm}^{-2}$  for the diffuse (6.0% of observed), and  $15.6 \text{ Wm}^{-2}$   
515 total flux (3.1% of observed). The good agreement between the calculated and observed  
516 fluxes indicates that the input parameters to the radiative transfer model are a reasonable  
517 approximation of the atmospheric state and aerosol properties.

518

519 These flux differences are consistent with values seen in previous aerosol radiative flux  
520 closure studies (Halothore and Schwartz 2000, Henzing 2004), despite the considerably

521 larger aerosol optical depths seen at Niamey. A more recent study, performed during a  
522 field experiment at the ARM Southern Great Plains (SGP) site in Oklahoma found  
523 smaller flux differences, with instantaneous biases in direct flux less than 1% and diffuse  
524 flux less than 2% (Michalsky et al. 2006). However, in the SGP study the radiometers  
525 were well-calibrated before the study and the aerosol properties were well characterized  
526 by in situ absorption and scattering measurements.

527

528 The calculated SW heating rate for the Jan 21 case study is shown in Figure 8a. The SW  
529 heating is concentrated in several layers in the troposphere, corresponding to moister  
530 layers identified from the sounding data (Figure 9). The SW heating is strongest in layers  
531 between 3-4 km and below 1 km, corresponding to the layers of strong aerosol extinction  
532 (Fig 6b). Above 5 km, SW heating is due primarily to water vapor absorption which  
533 begins to drop off above 8 km as the water vapor mixing ratio and effectiveness of water  
534 vapor absorption decrease.

535

536 As expected, the strongest aerosol heating is associated with the layers of high aerosol  
537 extinction (Fig 8b). The AER calculation assumed a constant lidar ratio for the entire  
538 aerosol column. In reality, we expect the biomass burning aerosol to be more absorbing  
539 than the dust aerosol, which would result in more absorption in the 3-4 km layer and  
540 reduce the absorption in the 0-1 km layer. The aerosol slightly increases the SW heating  
541 above 5 km due to SW radiation reflected from the top of the aerosol layer. Because of  
542 the bright surface and dry conditions at Niamey in January (PWV ~ 2.0 cm) this increase  
543 in absorption due to reflection from the aerosol layer is very small ( $< 0.05$  K/day per 100  
544 m layer). In a more humid atmosphere, the reflection from the aerosol layer would have  
545 a larger impact on heating and absorption above the layer due to increased water vapor  
546 absorption. Also, over a darker surface such as the ocean, rather than the highly  
547 reflecting surface at Niamey, the aerosol layer would have a larger impact on the total  
548 reflectance relative to clear sky.

549

550 **4.2. Aerosol direct radiative effect at the surface**

551 We extend the case-study analysis to examine the aerosol direct radiative effect at  
552 Niamey during the entire study period. All of the non-cloudy 15-minute periods are  
553 identified using the MPL and MFRSR cloud-screening methodologies. The calculated  
554 and observed downwelling surface fluxes show good agreement during non-cloudy  
555 periods, indicating reasonable confidence in the retrieved aerosol properties (Figure 10,  
556 Table 5).

557

558 We examine the aerosol radiative effect at the surface by subtracting the CLEAR  
559 calculation from the observed downwelling flux at the surface during non-cloudy periods  
560 (Fig 11). To remove the effect of the change in solar declination over the year, we  
561 normalize the flux difference by the incoming SW flux at the TOA. Aerosol reduces the  
562 direct SW flux at the surface relative to the CLEAR calculation because of the increased  
563 extinction. However, the increased scattering due to the aerosol layer increases the SW  
564 diffuse flux, which partially compensates for the reduced direct flux. In general, the  
565 direct effect is larger than the diffuse effect and the total SW radiative effect at the  
566 surface due to aerosol is negative. Positive total SW radiative effects are seen for some  
567 cases of small AOD (Fig 11c). These instances may be due to improper specification of  
568 the atmospheric state properties in the radiative transfer models or to errors in the  
569 observed fluxes. More cases with calculated positive aerosol radiative effects are  
570 observed during the Oct-Dec period, which may indicate issues with the instrumentation  
571 near the end of the field experiment. The calculated radiative effect is correlated strongly  
572 with the observed AOD, as expected. For the largest AOD values, aerosol reduces the  
573 total transmission at the surface by 30% relative to the CLEAR calculation. A linear fit of  
574 the change in total transmission (T) as a function of AOD, of the form  $\Delta T = 1 - a \cdot \text{AOD}$ , is  
575 calculated for each of the observed periods. The slope coefficients (a) are very similar for  
576 the two periods (0.12 for Jan-Apr and 0.13 for Oct-Dec).

577

578 The frequent presence of cirrus clouds during the dry season makes it difficult to examine  
579 the daily averaged aerosol radiative effect using the observed fluxes. Therefore we  
580 estimate the daily averaged aerosol radiative effect by subtracting the CLEAR calculation

581 from the AER calculation (in which the aerosol extinction and optical properties have  
582 been interpolated over cloudy periods). This calculation assumes that the aerosol does  
583 not vary over the cloudy periods. Since most of the cloudy periods during the dry season  
584 are due to high cirrus (above 8 km) we believe this is a reasonable assumption. We also  
585 estimate the daily averaged (24 hour) total radiative effect (aerosol + clouds) by  
586 subtracting the CLEAR calculation from the observed fluxes. A time series of the  
587 calculated daily averaged radiative effect is shown in Figure 12. The impact of clouds on  
588 the surface radiative effect can be seen by comparing the solid and dotted lines in the  
589 figure. The estimated average aerosol radiative effect is  $-27.9 \text{ W/m}^2$  per day ( $-108.7$   
590  $\text{W/m}^2$  direct flux and  $80.8 \text{ W/m}^2$  diffuse flux) while the average total radiative effect  
591 (including clouds and aerosol) is  $-35.1 \text{ W/m}^2$  day. Therefore, during the dry season at  
592 Niamey, aerosol accounts for about 80% of the observed SW radiative effect at the  
593 surface. The aerosol radiative effect at the surface is much stronger in the Jan-Apr  
594 period ( $-36.4 \text{ W/m}^2$ ) than in the Oct-Dec period ( $-14.6 \text{ W/m}^2$ ), due to the higher AOD and  
595 lower SSA in the Jan-Apr period.

596

597 This strong surface radiative effect of the aerosol has implications for the surface energy  
598 balance and boundary layer meteorology (Miller et al. 2004, 2008). Reduction of  
599 shortwave radiation absorbed at the surface can reduce the surface temperature and  
600 decrease the strength of boundary layer mixing. A reduction of latent heat flux beneath  
601 an aerosol layer could reduce large-scale precipitation. Miller et al. (2008) explored the  
602 role of aerosol radiative forcing on the surface energy balance over the seasonal cycle at  
603 Niamey. During the dry season, because of the limited column water vapor, the solar  
604 radiation at the surface was offset mainly by longwave radiation and the turbulent flux of  
605 sensible heat. Only during the rainy season did latent heat flux also play a role.

606

607 Due to the limited availability of ground-based observations, few constraints on model  
608 estimates of surface radiative effects due to mineral dust are available in this region.  
609 Model estimates of global SW surface radiative forcing due to mineral dust range from -  
610  $0.96 \text{ W/m}^2$  to  $-1.82 \text{ W/m}^2$  (Tegen et al. 1996, Woodward 2001, Miller et al. 2004)  
611 depending on details of the model's dust production and transport (prognostic or

612 specified) and assumptions about optical properties. Regional estimates of surface SW  
613 radiative forcing over North Africa range from roughly  $8 \text{ W/m}^2$  for yearly means (Tegen  
614 et al. 1996, Woodward 2001) to  $-25$  to  $-30 \text{ W/m}^2$  for Dec-Feb averages (Miller et al.  
615 2004). The observed aerosol radiative forcing at Niamey can help constrain and improve  
616 these model estimates of regional forcing.

617

618 Zhu et al. (2007) combined satellite estimates of AOD with a radiative transfer model to  
619 calculate the seasonal average radiative effect of dust over 3 regions. Off of the Saharan  
620 coast, they found a regional mean value of  $-23.0 \text{ W/m}^2$  SW at the surface averaged over  
621 the Jun-Aug period, which is slightly lower than our values. However, their Figure 9  
622 shows that larger values (up to  $-40 \text{ W/m}^2$ ) were found closer to the coastline. Christopher  
623 et al. (2003) calculated the aerosol surface radiative effect from ground-based  
624 observations of Saharan dust aerosol transported over the Atlantic to Puerto Rico. Their  
625 calculated daytime monthly mean SW aerosol radiative effect at the surface was  $-18$   
626  $\text{W/m}^2$ , which is significantly less than the value of  $-60 \text{ W/m}^2$  that we find if we calculate  
627 a daytime rather than 24-hour average radiative effect. The difference is due primarily to  
628 the reduced AOD (average of 0.26 in their study compared to 0.41 in our study) after  
629 transport across the Atlantic, but may also be due to differences in aerosol properties.

630

### 631 **4.3. Vertical Profiles of Aerosol Direct Radiative Effect**

632 Although several studies have examined the vertical profile and radiative properties of  
633 aged Saharan dust that has been transported across the Atlantic (Immler and Schrems  
634 2003; Leon et al. 2003) or across the Mediterranean (Mona et al. 2006), there has been  
635 little examination of vertical profiles of aerosol and radiative heating in the Sahel,  
636 because of the lack of vertically resolved measurements. As mentioned previously,  
637 Saharan aerosol that is transported across the Atlantic is usually in an elevated layer  
638 relative and thus can have significantly different structure in the vertical heating profile  
639 than dust aerosol over land closer to the dust source regions. Recent observations from a  
640 field campaign in southern Morocco (e.g., Ansmann et al. 2008) and from lidars deployed  
641 during the AMMA experiment (e.g. Heese et al. 2008) should significantly improve our

642 knowledge of the vertical profiles of aerosol properties and radiative effects over land  
643 and close to dust source regions.

644

645 Carlson and Benjamin (1980) calculated heating rates for idealized Saharan dust profiles  
646 over the desert and found SW heating (relative to clear sky) of 1.2 K/day with a fairly  
647 uniform heating profile from 500-1000 mb for an AOD of 1.0. Fouquart et al. (1987)  
648 used aircraft measurements of dust properties to calculate radiative heating profiles over  
649 Niamey. They found strong SW heating due to the dust in the lowest 2 km of the  
650 atmosphere, with a maximum value of 5 K/day (relative to clear sky) near noon on a day  
651 with AOD = 1.5 and 2 K/day near noon on a day with lower AOD (?).

652

653 Our results show strong SW heating due to aerosol in the lowest 4 km during the Jan-Apr  
654 period, with an average SW aerosol effect at 13:00 LST of 2.5 K/day near 500 m and 1  
655 K/day between 2-4 km (Fig 13). SW heating due to aerosol was significantly less in the  
656 Oct-Dec period, with maximum SW aerosol heating of 1 K/day near the surface and little  
657 aerosol heating above 2 km.

658

659 One uncertainty in the calculated heating rate profiles is the lack of knowledge of the  
660 vertical variability of the aerosol optical properties. From the MPL alone, discrimination  
661 between dust and biomass-burning aerosol layers is not possible. However, a ceilometer  
662 (1064 nm) was also part of the AMF deployment at Niamey. At these longer  
663 wavelengths, the ceilometer is less sensitive to the biomass burning aerosol than the MPL  
664 (Cattrall et al. 2005). Combination of the MPL and ceilometer data might allow  
665 discrimination between dust and biomass burning aerosol.

666

#### 667 **4.4. Uncertainty in Radiative Transfer Calculations**

668 Although there is good agreement with the direct flux, the case study shows a tendency  
669 for the model to slightly overestimate the diffuse flux. In this section we examine  
670 sources of uncertainty in the radiative transfer modeling, which include uncertainty in the  
671 input parameters (surface albedo, AOD, AP, SSA, PWV, ozone) and use of the Henyey-

672 Greenstein (HG) phase function in the flux calculations. Uncertainties in the aerosol  
673 optical properties come both from possible errors in the MFRSR-retrieved values and  
674 from extrapolation of the retrieved values to the wavelengths used in the RRTM model.

675

676 A sensitivity analysis was performed to determine the impact of changes to the input  
677 parameters on the calculated fluxes. Calculations for the Jan 21 cases were performed in  
678 which each of the above model input parameters was varied by 10%. Results of this  
679 sensitivity study are shown in Table 4. The direct flux is affected only by changes in  
680 AOD, PWV, and ozone, with AOD having the largest impact. A 10% change in AOD  
681 resulted in roughly a  $15 \text{ Wm}^{-2}$  change in direct flux, indicating that the mean direct flux  
682 could be matched by about a 3% reduction in AOD, which is within the estimated  
683 uncertainty. Changes in SSA had the largest effect on the modeled diffuse flux, with a  
684 10% reduction in SSA causing a  $26.8 \text{ W/m}^2$  (or 5.2%) reduction in modeled diffuse flux.  
685 Changes in asymmetry parameter and AOD also had significant impacts on the diffuse  
686 flux. Changes in surface albedo, ozone, and PWV had little effect on the diffuse flux,  
687 with changes of less than  $1.5 \text{ W/m}^2$  for each parameter. The sensitivity tests show that  
688 the diffuse flux could be easily matched by changes of about 5% in the retrieved SSA  
689 (Table 4).

690

691 In the flux calculations, a Henyey-Greenstein (HG) phase function (which depends only  
692 on the asymmetry parameter) is used. The HG phase function generally underestimates  
693 the forward scattering peak relative to a full Mie calculation and can affect the calculated  
694 aerosol radiative forcing (Boucher 1998). To test the effect of using the HG phase  
695 function, a sensitivity test was performed. For two different cases, representative size  
696 distributions and imaginary values of the refractive index were saved from the MFRSR  
697 retrievals. The refractive index was extrapolated to the RRTM wavelengths and Mie  
698 calculations were performed using the retrieved size distribution to calculate the AP,  
699 SSA, and full phase function. Then flux calculations were performed using the  
700 calculated SSA and AP and either the full Mie phase function or the HG approximation.  
701 For each of the two periods, which had effective radius of  $0.68\mu\text{m}$  and  $0.77\mu\text{m}$ ,  
702 respectively, the use of the full phase function increased the diffuse flux at the surface by

703 less than  $1.5 \text{ W/m}^2$  compared to the calculations with the HG phase function. Although  
704 larger differences between the full phase function and HG phase function are expected  
705 for larger particles that are observed during fresh dust events, this analysis indicates that  
706 use of the HG phase function is not a large source of uncertainty for this study.

707

708 An additional source of uncertainty in both the MFRSR AOD retrievals and the flux  
709 closure comparisons is due to the geometry of the MFRSR and the broadband  
710 radiometers and the partitioning of the direct and diffuse fluxes. Theoretically, the SW  
711 direct flux is that part of the incoming solar radiation that has not been scattered while the  
712 diffuse component consists of light that has been scattered at least once. In radiative  
713 transfer model calculations, these contributions can be easily separated. However in  
714 observations it is not as straightforward to estimate or remove contributions from the  
715 solar aureole, or forward scattering into the instrument field of view. The MFRSR uses a  
716 shadow-band to block the sun for the diffuse sky measurement, and takes two sideband  
717 measurements to estimate the solar aureole contribution to the blocked measurement. As  
718 aerosol effective radius increases, and forward scattering contributions become more  
719 important, the underestimate of the solar aureole contribution increases (Alexandrov et al.  
720 2007).

721

722 Russell et al. (2004) estimate the contribution of forward scattering by dust aerosols to  
723 sun photometer and pyrliometer measurements as a function of field of view. For  
724 instruments with half-angle  $\eta = 1.85^\circ$ , AOD correction factors at 354 nm can be as large  
725 as 10%, and for  $\eta = 2.8^\circ$  they can be up to 16%. Comparison of the MFRSR retrieved  
726 AODs to values from a narrow field of view ( $\eta < 1^\circ$ ) sun photometer that was collocated  
727 at the Niamey site during the latter half of the year, indicate that the MFRSR  
728 underestimates AOD by around 15% compared to the sun photometer due to the forward  
729 scattering effect. A correction for the effect of large particle scattering on the MFRSR  
730 retrievals at Niamey, taking into account the MFRSR shadowband geometry and the  
731 aerosol Angstrom coefficient, is under development but is not yet available (C. Flynn,  
732 personal communication, 2008).

733

734 The NIP instrument also has a relatively large field of view,  $\eta = 2.8^\circ$ , and the shading  
735 disk for the shaded pyranometer was designed to have the same geometry. Due to the  
736 similar effective fields of view of the NIP, shaded PSP, and MFRSR, the under-estimate  
737 of AOD from the MFRSR is partially compensated for by an over-estimate of direct flux  
738 from the NIP and under-estimate of diffuse flux from the PSP, which explains the good  
739 agreement in the radiative transfer calculations. In the future, if the AODs measured by  
740 the MFRSR are corrected for forward scattering, then the NIP and shaded PSP must also  
741 be corrected to examine flux closure of the direct and diffuse components.  
742

## 743 **5.0 Summary and Conclusions**

744  
745 The AMF deployment in Niamey, Niger provided an unprecedented opportunity to study  
746 aerosol properties and the aerosol surface radiative effects in the Sahel. We used MFRSR  
747 measurements to retrieve aerosol optical properties, including optical depth, single  
748 scattering albedo, and asymmetry parameter during the dry seasons at Niamey. The co-  
749 located MPL allowed us to estimate the vertical distribution of the aerosol extinction.  
750 Using the retrieved aerosol properties and vertical extinction profiles, we calculated the  
751 broadband fluxes and heating rates at Niamey.

752  
753 The retrieved aerosol optical properties were compared to values from the literature as  
754 well as values from aircraft profiles over Niamey in Jan-Feb as part of the DABEX  
755 experiment. The single scattering albedo showed strong absorption at shorter  
756 wavelengths, which decreased with increasing wavelength, indicating the presence of  
757 iron oxides in the dust aerosol. The range in single scattering albedo from the MFRSR  
758 retrievals agreed well with the DABEX aircraft measurements, although the SSA were  
759 significantly lower than in previous observations of Saharan dust. The DABEX flights  
760 indicated that the lower SSA values were due to biomass burning aerosol layers that were  
761 prevalent during the first part of the year. The SSA values were much higher in the Oct-  
762 Dec time period, although there were still occasions when they were lower than would be  
763 expected for pure dust, which may be due to local combustion sources near Niamey or

764 variations in mineral content. Along with the optical properties, the vertical profiles  
765 were also seen to vary between the two study periods, with the aerosol extinction  
766 concentrated in a shallower layer during Oct-Dec.

767

768 Comparison of the calculated surface fluxes to observed fluxes for non-cloudy periods  
769 indicated that the remote sensing retrievals provided a reasonable estimation of the  
770 optical properties. The calculations tended to underestimate the diffuse flux relative to  
771 the observations for higher AOD values. This difference is likely due to the fact that  
772 small uncertainties in the aerosol property retrievals are magnified as the aerosol loading  
773 increases. Sensitivity tests for the case study calculations showed that we were able to  
774 match the observed fluxes with variations of < 10% in the inputs to the radiative transfer  
775 model. For example, a 5% reduction of SSA brought the calculated diffuse flux in very  
776 good agreement (~1%) with the observed flux.

777

778 We calculated the instantaneous direct aerosol radiative effect at the surface by  
779 subtracting the CLEAR calculation from the observed fluxes. Reduction in the SW  
780 direct flux due to aerosol extinction was partially compensated for by increases in diffuse  
781 flux to aerosol scattering, however the net SW radiative effect was to reduce SW  
782 insolation at the surface. The magnitude of the direct radiative effect was strongly related  
783 to aerosol optical depth, but also depends on time of day and aerosol optical properties.  
784 The maxim value of the instantaneous SW aerosol radiative effect was  $-366 \text{ W/m}^2$ , which  
785 occurred during the dust storm on March 6, 2006. We estimated the daily-averaged  
786 aerosol radiative effect at the surface by subtracting the CLEAR calculation from the  
787 AER calculation. The average SW aerosol radiative effect over the study period was  $-27$   
788  $\text{W/m}^2$ , which is comparable to values estimated from satellite data and from climate  
789 models with sophisticated dust parameterizations.

790

791 Uncertainty in the derived extinction profiles and corresponding radiative heating  
792 calculations is caused by the inability to distinguish between the dust and biomass  
793 burning aerosol. Application of multi-wavelength lidar might allow discrimination and  
794 improve the representation of the vertical profile. Additionally, combination of the

795 MFRSR, which is more sensitive to the fine mode aerosol, with longwave sensors such as  
796 the AERI, which is more sensitive to the coarse mode aerosol, could help identify the  
797 relative contribution of dust and biomass burning aerosol to the total column extinction.

798

799 Acknowledgements

800

801 The AMF was deployed to Niamey as part of the RADAGAST project through funding  
802 from the Atmospheric Radiation Measurement (ARM) Program, Office of Biological and  
803 Environment Research, U.S. Department of Energy. We thank Tony Slingo, the  
804 RADAGAST principal investigator; Mark Miller, the AMF lead scientist; and everyone  
805 else whose hard work contributed to the successful AMF deployment. We also thank  
806 Dave Turner for providing the MWR retrievals and Jim Mather for the merged sounding  
807 profiles. Funding for this project was provided by the U.S. Department of Energy, Office  
808 of Science, as part of the ARM program under contract DE-AC06-76RL01830 to PNNL.  
809 PNNL is operated by Battelle for the U.S. Dept. of Energy.

## References

- Alexandrov, M. D., Kiedron, P., Michalsky, J. J., Hodges, G., Flynn, C. J., and Lacis, A. A. (2007), Optical depth measurements by shadow-band radiometers and their uncertainties, *Appl. Opt.*, 46 (33).
- Alfaro, S.C., S. Lafon, J.L. Rajot, P. Formenti, A. Gaudichet, and M. Maille (2004), Iron oxides and light absorption by pure desert dust: An experimental study. *J. Geophys. Res.*, 109, D08208.
- Ansmann, A., M. Tesche, D. Althausen, D. Muller, P. Seifert, V. Freudenthaler, B. Heese, M. Wiegner, G. Pisani, P. Knippertz, and O. Dubovik (2008), Influence of Saharan dust on cloud glaciation in southern Morocco during SAMUM. *J. Geophys. Res.*, *in press*.
- Boucher, O. (1998), On aerosol direct shortwave radiative forcing and the Henyey-Greenstein phase function. *J. Atmos. Sci.*, 55, 128-134.
- Campbell, J. R., D. L. Hlavka, E. J. Welton, C. J. Flynn, D. D. Turner, J. D. Spinhirne, V. S. Scott and I. H. Hwang (2002), Full-Time, Eye-Safe Cloud and Aerosol Lidar Observation at Atmospheric Radiation Measurement Program Sites: Instruments and Data Processing, *Journal of Atmospheric and Oceanic Technology*, 19(4), 431-442.
- Carlson, T.N. and S.G. Benjamin (1980), Radiative heating rates for Saharan dust. *J. Atmos. Sci.*, 37, 193-213.
- Cattrell, C., J. Reagan, K. Thome, and O. Dubovik (2005), Variability of aerosol and spectral lidar and backscatter and extinction ratios of key aerosol types derived from selected Aerosol Robotic Network locations. *J. Geophys. Res.*, 110, doi:10.1029/2004JD005124.
- Christopher, S.A., J. Wang, Q. Ji, and S.C. Tsay (2003), Estimation of diurnal shortwave dust aerosol radiative forcing during PRIDE. *J. Geophys. Res.*, 108 (19), 8596.
- Clough, S.A., M.W. Shephard, E.J. Mlawer, J.S. Delamere, M.J. Iacono, K. Cady-Pereira, S. Boukabara, P.D. Brown (2005), Atmospheric radiative transfer modeling: a summary of the AER codes. *Journal of Quantitative Spectroscopy & Radiative Transfer*, 91, 233-244.

- Dubovik, O., A. Sinyuk, T. Lapyonok, B.N. Holben, M. Mishchenko, P. Yang, T.F. Eck, H. Volten, O. Muñoz, B. Veihelmann, W.J. van der Zande, J.-F. Leon, M. Sorokin, and I. Slutsker (2006), Application of spheroid models to account for aerosol particle nonsphericity in remote sensing of desert dust. *J. Geophys. Res.*, 111, D11208, doi:10.1029/2005JD006619.
- Dunion, J. P. and C. S. Velden (2004), The impact of the Saharan air layer on Atlantic tropical cyclone activity, *Bulletin of the American Meteorological Society*, 85(3), 353-364.
- Evans, K. F. (1998), The spherical harmonics discrete ordinate method for three-dimensional atmospheric radiative transfer, *Journal of the Atmospheric Sciences*, 55(3), 429-446.
- Fernald, F.G. (1984), Analysis of atmospheric lidar observations. *Appl. Opt.*, 23
- Fouquart, Y., B. Bonnel, G. Brogniez, J.C. Buriez, L. Smith, J.J. Morcrette, and A. Cerf (1987), Observations of Saharan aerosols: Results of ECLATS field experiment. Part II: Broadband radiative characteristics of the aerosols and vertical radiative flux divergence. *J. Clim. Appl. Met.*, 26, 38-52.
- Halothore, R.N. and S.E. Schwartz (2000), Comparison of model-estimated and measured diffuse downward irradiance at the surface in cloud-free skies. *J. Geophys. Res.*, 105, 20165-20177.
- Harries, J.E. et al. (2005), The Geostationary Earth Radiation Budget (GERB) experiment. *Bull. Am. Meteorol. Soc.*, 86, 945-960.
- Harrison, L. and J. Michalsky (1994), Objective Algorithms for the Retrieval of Optical Depths from Ground-Based Measurements, *Applied Optics*, 33(22), 5126-5132.
- Haywood, J. M., R. P. Allan, I. Culverwell, T. Slingo, S. Milton, J. Edwards and N. Clerbaux (2005), Can desert dust explain the outgoing longwave radiation anomaly over the Sahara during July 2003?, *J. Geophys. Res.-Atmos.*, 110(D5).
- Haywood, J. M., P. Francis, S. Osborne, M. Glew, N. Loeb, E. Highwood, D. Tanre, G. Myhre, P. Formenti and E. Hirst (2003), Radiative properties and direct radiative effect of Saharan dust measured by the C-130 aircraft during SHADE: Solar spectrum, *J. Geophys Res-Atmos*, 108(18).

- Heese, B. and M. Wiegner (2008), Vertical aerosol profiles from Raman-depolarization lidar observations during the dry season AMMA field campaign. *Submitted to J. Geophys. Res., DABEX Special Issue.*
- Henzing, J.S., et al. (2004), Effect of aerosols on the downward shortwave irradiances at the surface: Measurements versus calculations with MODTRAN4.1, *J. Geophys. Res.*, 109, D14204, doi:10.1029/2003JD004142.
- Highwood, E. J., J. M. Haywood, M. D. Silverstone, S. M. Newman and J. P. Taylor (2003), Radiative properties and direct effect of Saharan dust measured by the C-130 aircraft during Saharan Dust Experiment (SHADE): 2. Terrestrial spectrum, *Journal of Geophysical Research-Atmospheres*, 108(D18).
- Idso, S.B., R.D. Jackson, R.J. Reginato, B.A. Kimball, and F.S. Nakayma (1975), The dependence of bare soil albedo on soil water content. *J. Appl. Met.*, 14, 109-113.
- Johnson, B.T., S.R. Osborne, J.M. Haywood, and M.A.J. Harrison (2008a), Aircraft measurements of biomass burning aerosols over West Africa during DABEX. *Submitted to J. Geophys. Res., DABEX Special Issue.*
- Johnson, B.T., B. Heese, S.A. McFarlane, P.Chazette, A. Jones, and N. Bellouin (2008b), Vertical distribution and radiative forcing of mineral dust and biomass-burning aerosols over West Africa during DABEX. *J. Geophys. Res., DABEX Special Issue, Accepted.*
- Kahn, R., R. West, D. McDonald, B. Rheingans, and M.I. Mishchenko, 1997: Sensitivity of multiangle remote sensing observations to aerosol sphericity. *J. Geophys. Res.*, 102, 16861-16870, doi:10.1029/96JD01934.
- Kassianov, E.I., C.J. Flynn, T.P. Ackerman, and J.C. Barnard, 2007: Aerosol Single-Scattering Albedo and Asymmetry Parameter from MFRSR Observations during the ARM Aerosol IOP 2003, *Atmospheric Chemistry and Physics*, 7(12):3341-3351.
- Kaufman, Y. J., D. Tanre, O. Dubovik, A. Karnieli, and L.A. Remer (2001), Absorption of sunlight by dust as inferred from satellite and ground-based remote sensing. *Geophys. Res. Lett.*, 28, 1479-1483.

- Koven, C.D. and I. Fung (2006), Inferring dust composition from wavelength-dependent absorption in Aerosol Robotic Network (AERONET) data. *J. Geophys. Res.*, 111, D14205, doi:10.1029/2005JD006678.
- Li, F., A.M. Vogelmann, and V. Ramanathan (2004), Saharan dust aerosol radiative forcing measured from space. *J. Clim.*, 17(13), 2558-2571.
- Mahowald, N. M., G. D. R. Rivera, and C. Luo (2004), Comment on “Relative importance of climate and land use in determining present and future global soil dust emission” by I. Tegen et al., *Geophys. Res.Lett.*, 31, L24105, doi:10.1029/2004GL021272.
- Mather, J. H., S. A. McFarlane, M. A. Miller and K. L. Johnson (2007), Cloud properties and associated radiative heating rates in the tropical western Pacific, *Journal of Geophysical Research-Atmospheres*, 112(D5).
- McFarlane, S. A. and K. F. Evans (2004), Clouds and shortwave fluxes at Nauru. Part II: Shortwave flux closure, *Journal of the Atmospheric Sciences*, 61(21), 2602-2615.
- Michalsky, J. J., Schlemmer, J. A., Berkheiser, W. E., Berndt, J. L., Harrison, L. C., Laulainen, N. S., Larson, N. R., and Barnard, J. C. (2001): Multi-year measurements of aerosol optical depth in the atmospheric radiation measurement and quantitative links programs., *J. Geophys. Res.*, 106 (D11), 12099-12107.
- Michalsky J.J., G. P. Anderson, J. Barnard, J. Delamere, C. Gueymard, S. Kato, P. Kiedron, A. McComiskey, and P. Ricchiazzi (2006), Shortwave radiative closure studies for clear skies during the Atmospheric Radiation Measurement 2003 Aerosol Intensive Observation Period, *J. Geophys. Res.*, 111, D14S90, doi:10.1029/2005JD006341.
- Miller, R.L., I. Tegen, and J. Perlwitz (2004), Surface radiative forcing by soil dust aerosols and the hydrologic cycle. *J. Geophys. Res.*, 104, D404203, doi:10.1029/2003JD004085.
- Miller, M. A. and A. Slingo, The Atmospheric Radiation Measurement (ARM) Mobile Facility (AMF) and its First International Deployment: Measuring Radiative Flux Divergence in West Africa (2007), *Bull. Amer. Met. Soc.*, 88(8), 1229-1244.
- Mishchenko, M.I., L.D. Travis, R.A. Kahn, and R.A. West, 1997: Modeling phase functions for dustlike tropospheric aerosols using a mixture of randomly oriented

- polydisperse spheroids. *J. Geophys. Res.*, **102**, 16831-16847, doi:10.1029/96JD02110.
- Osborne, S.R., B. T. Johnson, J. M. Haywood, and C. L. McConnell, Physical and optical properties of mineral dust aerosol during the Dust and Biomass-burning Experiment (DABEX) (2008), *Submitted to J. Geophys. Res.*
- Pal, S., W. Steinbrecht, and A. Carswell (1992), Automated method for lidar determination of cloud-base and vertical extent. *Appl. Optics*, 31, 1488-1494.
- Prospero, J. M. and P. J. Lamb (2003), African droughts and dust transport to the Caribbean: Climate change implications, *Science*, 302(5647), 1024-1027.
- Prospero, J.M., and T.N. Carlson (1981), Saharan air outbreaks over the tropical North Atlantic, *Pure Appl. Geophys.*, 119, 677-691.
- Redelsperger, J.L., C.D. Thorncroft, A. Diedhiou, T. Lebel, D.J. Parker, and J. Polcher (2006), African monsoon multidisciplinary analysis – An international research project and field campaign. *Bull. Amer. Met. Soc.*, 87(12), 1739-1746.
- Schmetz, J. P. Pili, S. Tjemkes, D. Just, J. Kerkman, S. Rota, and A. Ratier (2002), An introduction to Meteosat Second Generation (MSG). *Bull. Amer. Meteor. Soc.*, 83, 977-992.
- Settle, J.J., N.A. Bharmal, G.J. Robinson, A. Slingo (2008), Bounding the uncertainty of flux divergence calculations in RADAGAST. *In preparation for J. Geophys. Res., RADAGAST special issue.*
- Slingo, A., T.P. Ackerman, R.P. Allan, E.I. Kassianov, S.A. McFarlane, G.J. Robinson, J.C. Barnard, M.A. Miller, J.E. Harries, J.E. Russell, S. Dewitte (2006), Observations of the impact of a major Saharan dust storm on the Earth's radiation budget. *Geophys. Res. Lett.*, 33, L24817, doi:10.1029/2006GL027869.
- Slingo, A. et al. (2008a), Overview of observations from the RADAGAST experiment in Niamey, Niger. Part 1: Meteorology and thermodynamic variables. *Submitted to J. Geophys. Res., RADAGAST special issue.*
- Slingo, A. et al. (2008b), Overview of observations from the RADAGAST experiment in Niamey, Niger. Part 2: Radiative fluxes and divergences. *In preparation for J. Geophys. Res., RADAGAST special issue.*

- Sokolik, I.N. and O.B. Toon (1999), Incorporation of mineralogical composition into models of the radiative properties of mineral aerosol from UV to IR wavelengths. *J. Geophys. Res.*, 104, 9423-9444.
- Tanre, D. et al., 1986, Simulation of the satellite signal in the solar spectrum (5S), Laboratoire d'Optique Atmospherique, 262 pp.
- Tegen, I., A. A. Lacis, and I. Fung (1996), The influence on climate forcing of mineral aerosols from disturbed soils, *Nature*, 380, 419 – 422.
- Turner, D.D. (2008), Ground-based Infrared Retrievals of Optical Depth, Effective radius and composition of airborne mineral dust above the Sahel. *Submitted to J. Geophys. Res., RADAGAST Special Issue.*
- Welton, E. J., K. J. Voss, H. R. Gordon, H. Maring, A. Smirnov, B. Holben, B. Schmid, J. M. Livingston, P. B. Russell, P. A. Durkee, P. Formenti and M. O. Andreae (2000), Ground-based lidar measurements of aerosols during ACE-2: instrument description, results, and comparisons with other ground-based and airborne measurements, *Tellus Series B-Chemical and Physical Meteorology*, 52(2), 636-651.
- Welton, E.J. and J.R. Campbell, 2002, Micropulse lidar signals: uncertainty analysis. *J. Atmos. Ocean. Tech.*, 19, 2089-2094.
- Wild, M., C. N. Long and A. Ohmura (2006), Evaluation of clear-sky solar flux in GCMs participating in AMIP and IPCC-AR4 from a surface perspective, *Journal of Geophysical Research-Atmospheres*, 111(D1).
- Yang, P., Q. Feng, G. Hong, G.W. Kattawar, W.J. Wiscombe, M.I. Mishchenko, O. Dubovik, I. Laszlo, and I.N. Sokolik, 2007: Modeling of the scattering and radiative properties of nonspherical dust-like aerosols. *J. Aerosol Sci.*, **38**, 995-1014, doi:10.1016/j.jaerosci.2007.07.001.
- Zhu, A., V. Ramanathan, L. Fang, and D. Kim (2007), Dust plumes over the Pacific, Indian, and Atlantic oceans: Climatology and radiative impact. *J. Geophys. Res.*, 112, D16208, 2007JD008427.

### Table Captions

Table 1. Statistics of average retrieved aerosol optical properties during each period.

Table 2. Variability in aerosol optical properties at 500 nm between the two dry periods.

Table 3. Statistics of calculated and observed fluxes for Jan 21 case study. All averages are taken over daylight times (solar zenith angle  $> 0^\circ$ ).

Table 4. Average fluxes over daylight period for Jan 21 case. The observed fluxes and original AER calculated fluxes are given in the top two rows. Calculated fluxes based on changing a single parameter by the stated amount are given in the remainder of the table. Difference in sensitivity test fluxes minus original AER calculated fluxes is given in parentheses for each sensitivity test.

### Figure Captions

Figure 1. Time-series of daily-average broadband albedo measured at the Niamey airport and Banizoumbou sites.

Figure 2. Time series of daily-averaged cloud-screened AOD at 500 nm retrieved from the MFRSRs at the Niamey airport and Banizoumbou.

Figure 3. Time series of daily-averaged cloud-screened a) Angstrom exponent, b) asymmetry parameter, and c) single scattering albedo retrieved from the MFRSR at the Niamey site. Angstrom exponent retrieved at the Banizoumbou site is also shown in the top panel.

Figure 4. Curtain plot of cloud-screened aerosol extinction derived from MPL at Niamey. In periods of very optically thick aerosol (such as day 65), lidar is attenuated and cannot see the entire column.

Figure 5. Average vertical profile of cloud-screened aerosol extinction derived from MPL for the entire study period (thick black line) and for each month separately.

Figure 6. a) MPL corrected backscatter (relative units) and b) MPL-derived extinction profile for Jan 21 case study. Missing backscatter data near 12 UTC is due to closure of the MPL shutter to protect the optics; extinction profiles are interpolated over this period.

Figure 7. Observed and calculated a) shortwave total, b) diffuse, and c) direct fluxes at the surface for the Jan 21 case study. AER calculations include aerosol, but no clouds. CLEAR calculations use same atmospheric state inputs but have no aerosol.

Figure 8. a) Calculated shortwave heating rate profile for Jan 21 case study. b) Aerosol effect on shortwave heating profile, defined as AER-CLEAR. Note log scale in lower panel.

Figure 9. Average a) temperature and b) water vapor mixing ratio profiles derived from radiosonde data from Jan 21, 2006.

Figure 10. Comparison of calculated and measured a) direct, b) diffuse, and c) total downwelling shortwave fluxes at the surface for all non-cloudy 15 minute periods. Values given in each figure are mean observed flux, mean flux difference (AER-OBS), and RMS flux difference, respectively.

Figure 11. Normalized radiative effect of aerosols on downwelling SW at the surface for non-cloudy periods for a) direct SW, b) diffuse SW, and c) total SW. Normalized flux difference is calculated as the observed downwelling flux at the surface (OBS) minus the

calculated downwelling flux at the surface (CLEAR) divided by incoming SW flux at the top of the atmosphere. Linear fit lines are described in the text.

Figure 12. Time series of daily-averaged aerosol SW total (solid), direct (dashed) and diffuse (dashed-dotted) radiative forcing at the surface. Also included on the plot is the estimated daily-averaged aerosol + cloud total SW radiative forcing (blue) and the daily-averaged AOD (red). Note the discontinuity in the time axis.

Figure 13. Average a) cloud-screened heating rate and b) extinction profile at 13:00 local time for Jan-Apr and Oct-Dec dry periods.

Wavelength (nm)	Jan-Apr			Oct-Dec		
	AOD	AP	SSA	AOD	AP	SSA
415	0.58	0.70	0.82	0.36	0.70	0.90
500	0.53	0.67	0.94	0.33	0.67	0.99
615	0.50	0.65	0.98	0.30	0.67	0.99
673	0.48	0.65	0.97	0.29	0.67	0.99
870	0.44	0.64	0.97	0.27	0.67	0.99
Angstrom Parameter	0.48			0.47		

Table 1. Statistics of average retrieved aerosol optical properties during each period.

Properties at 500 nm	Jan-Apr			Oct-Dec		
	AVG	MIN	MAX	AVG	MIN	MAX
AOD	0.53	0.12	3.57	0.33	0.07	1.63
AP	0.67	0.58	0.74	0.67	0.61	0.75
SSA	0.94	0.73	1.00	0.99	0.82	1.00

Table 2. Variability in aerosol optical properties at 500 nm between the two dry periods.

	Total SW Flux (Wm <sup>-2</sup> )	Diffuse SW Flux (Wm <sup>-2</sup> )	Direct SW Flux (Wm <sup>-2</sup> )
Mean Observed	497.0	193.4	303.6
Mean AER	512.6	205.0	307.7
Mean CLEAR	588.5	49.5	539.0
Mean Difference (AER-OBS)	15.6	11.6	4.1
Max Difference  AER-OBS	28.7	30.0	13.7

Table 3. Statistics of calculated and observed fluxes for Jan 21 case study. All averages are taken over daylight times (solar zenith angle > 0°).

	Parameter	Change in Parameter	SW Total (Wm <sup>-2</sup> )	SW Diffuse (Wm <sup>-2</sup> )	SW Direct (Wm <sup>-2</sup> )
Observed	-	-	497.0	193.4	303.6
AER Calculation	-	-	512.6	205.0	307.7
Sensitivity Tests	PWV	+10%	509.9 (-2.7)	204.1 (-0.9)	305.8 (-1.9)
		-10%	515.5 (2.9)	205.8 (0.8)	309.7 (2.0)
	Ozone	+10%	511.7 (-0.9)	204.4 (-0.6)	307.2 (-0.5)
		-10%	513.6 (1.0)	205.5 (0.5)	308.1 (0.4)
	Surface Albedo	+10%	514.1 (1.5)	206.5 (1.5)	307.7 (0)
		-10%	511.1 (-1.5)	203.5 (-1.5)	307.7 (0)
	AOD	+10%	505.9 (-6.7)	213.8 (8.8)	292.1 (-15.6)
		-10%	519.5 (6.9)	195.3 (-9.7)	324.2 (16.5)
	AP	+10%	519.4 (6.8)	211.8 (6.8)	307.7 (0)
		-10%	506.2 (-6.4)	198.5 (-6.5)	307.7 (0)
	SSA	+10%	535.4 (22.8)	227.8 (22.8)	307.7 (0)
		-10	485.8 (-26.8)	178.1 (-26.8)	307.7 (0)
		-5	498.9 (-13.7)	191.2 (-13.7)	307.7 (0)

Table 4. Average fluxes over daylight period for Jan 21 case. The observed fluxes and original AER calculated fluxes are given in the top two rows. Calculated fluxes based on changing a single parameter by the stated amount are given in the remainder of the table. Difference in sensitivity test fluxes minus original AER calculated fluxes is given in parentheses for each sensitivity test.

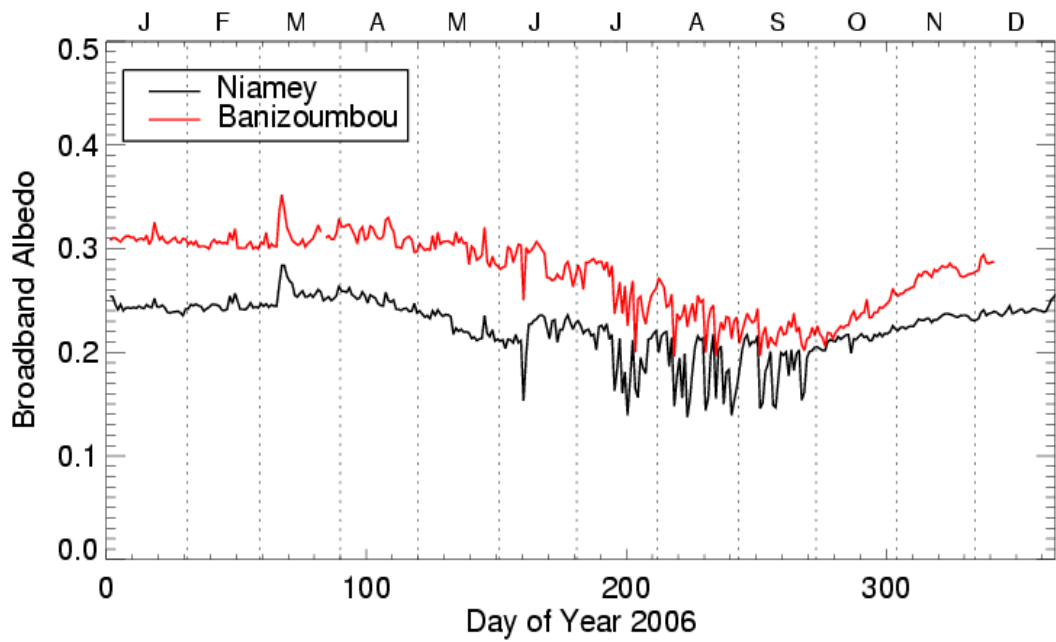


Figure 1. Time-series of daily-average broadband albedo measured at the Niamey airport and Banizoumbou sites.

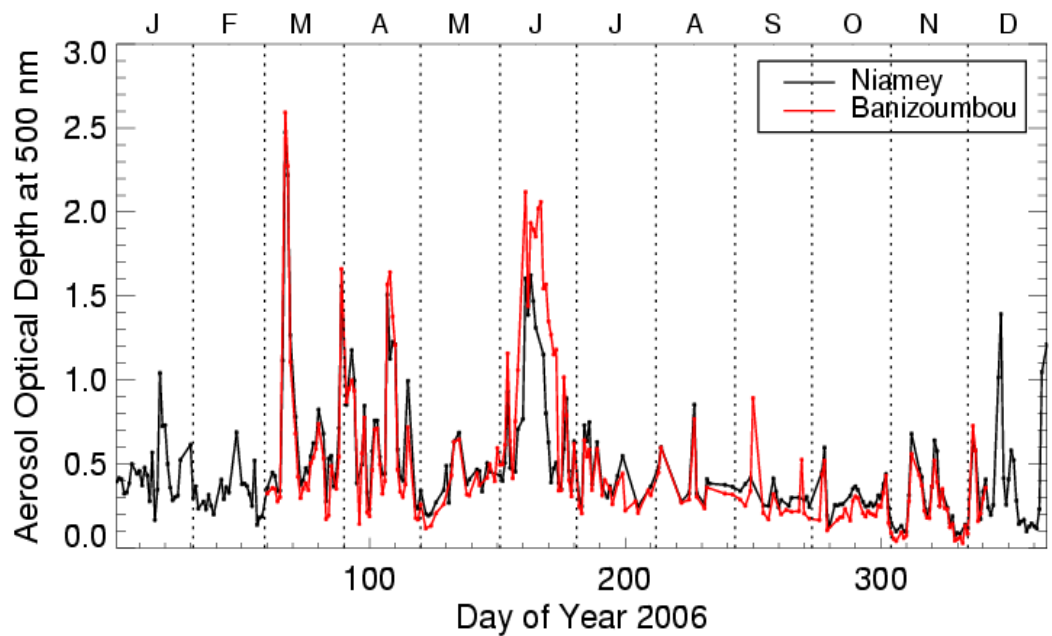


Figure 2. Time series of daily-averaged cloud-screened AOD at 500 nm retrieved from the MFRSRs at the Niamey airport and Banizoumbou.

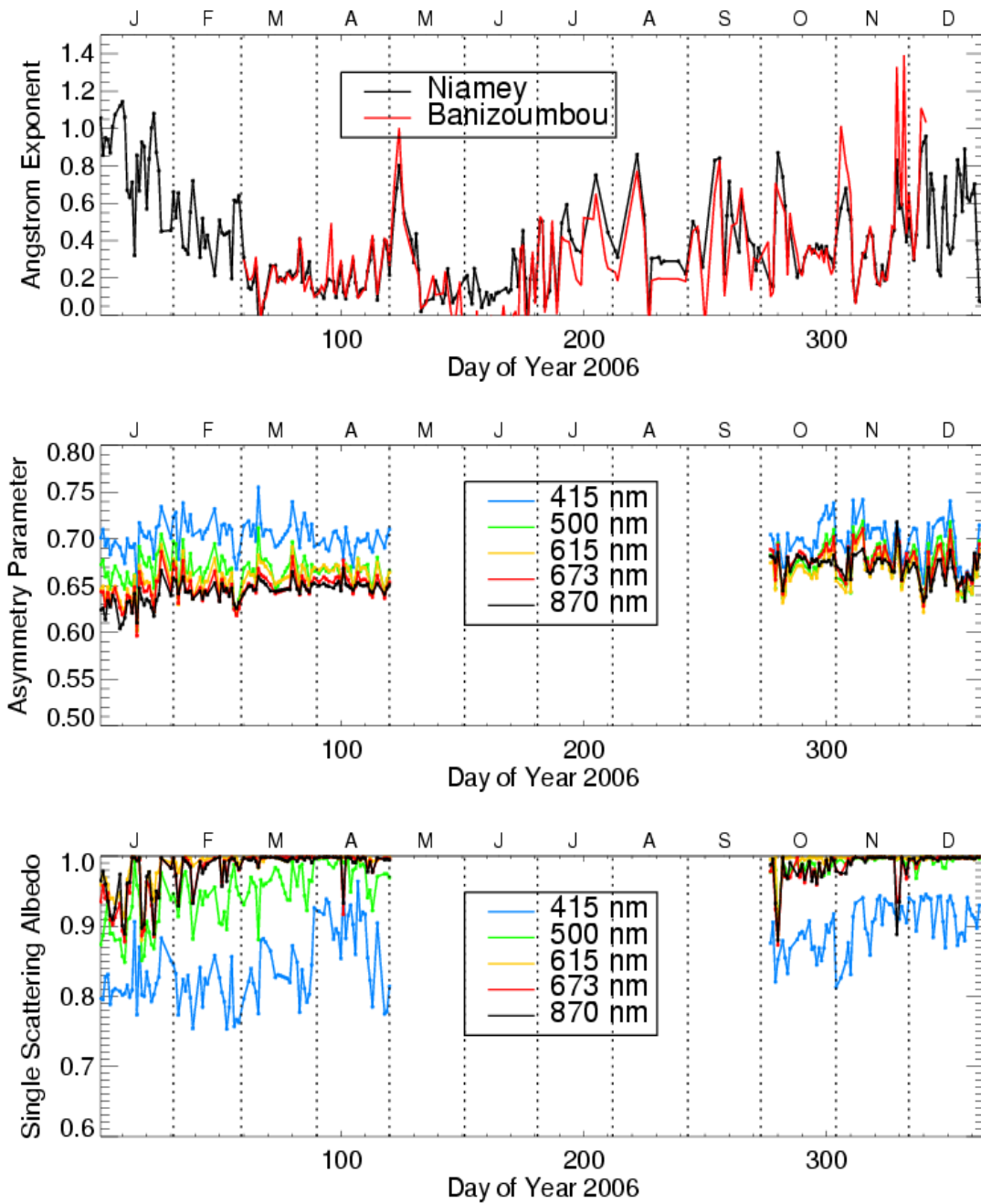


Figure 3. Time series of daily-averaged cloud-screened a) Angstrom exponent, b) asymmetry parameter, and c) single scattering albedo retrieved from the MFRSR at the Niamey site. Angstrom exponent retrieved at the Banizoumbou site is also shown in the top panel.

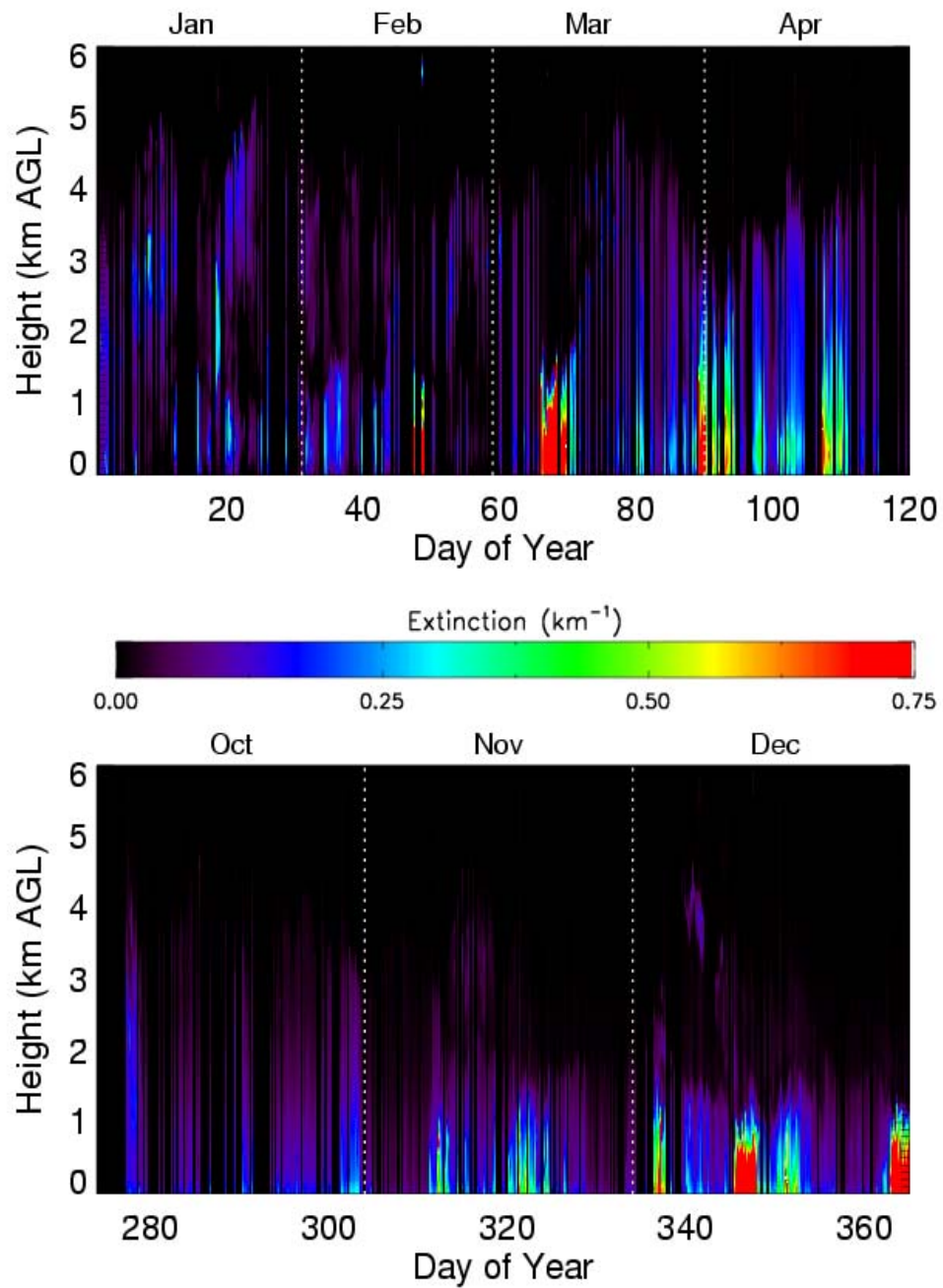


Figure 4. Curtain plot of cloud-screened aerosol extinction derived from MPL at Niamey. In periods of very optically thick aerosol (such as day 65), lidar is attenuated and cannot see the entire column.

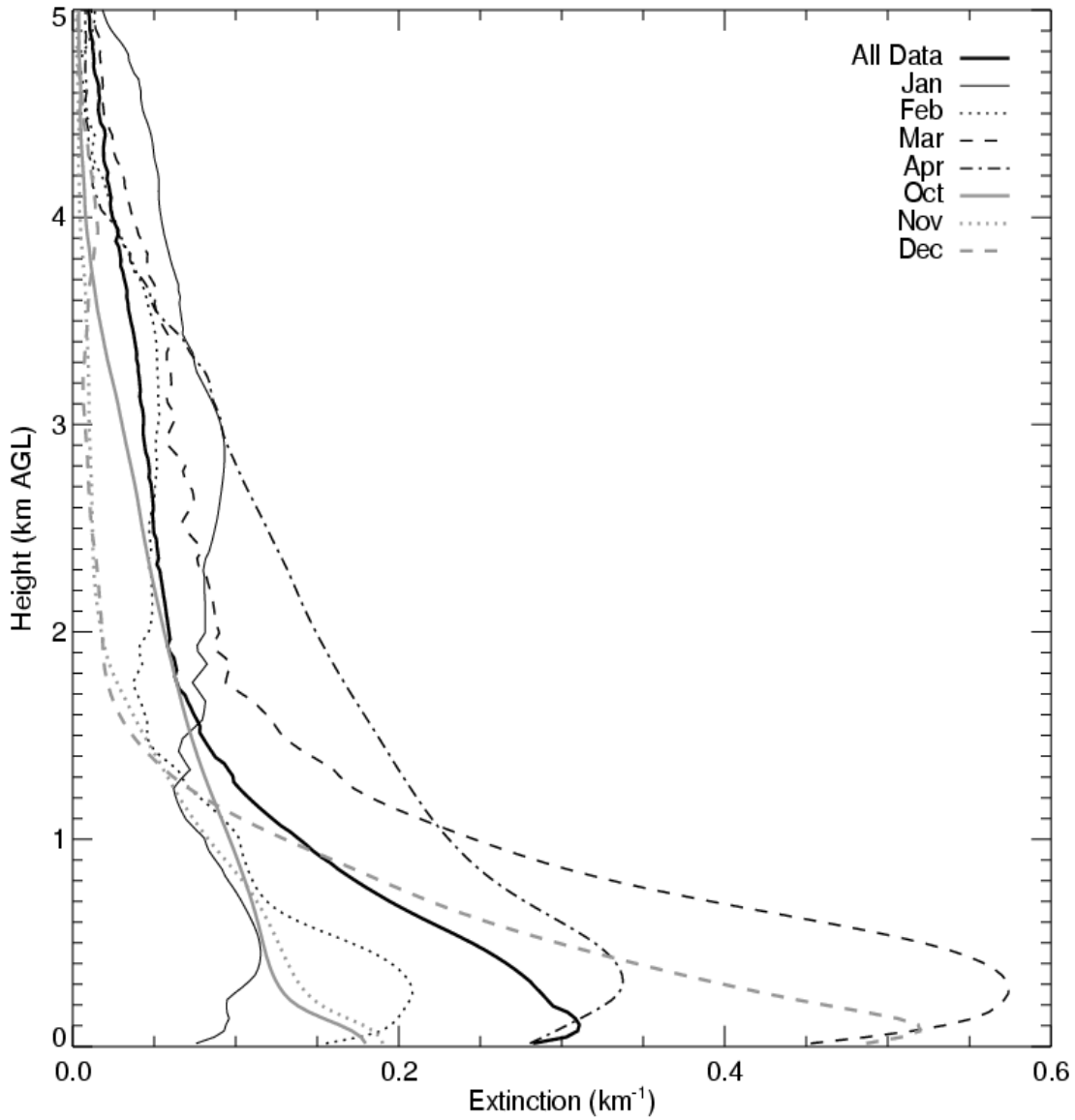


Figure 5. Average vertical profile of cloud-screened aerosol extinction derived from MPL for the entire study period (thick black line) and for each month separately.

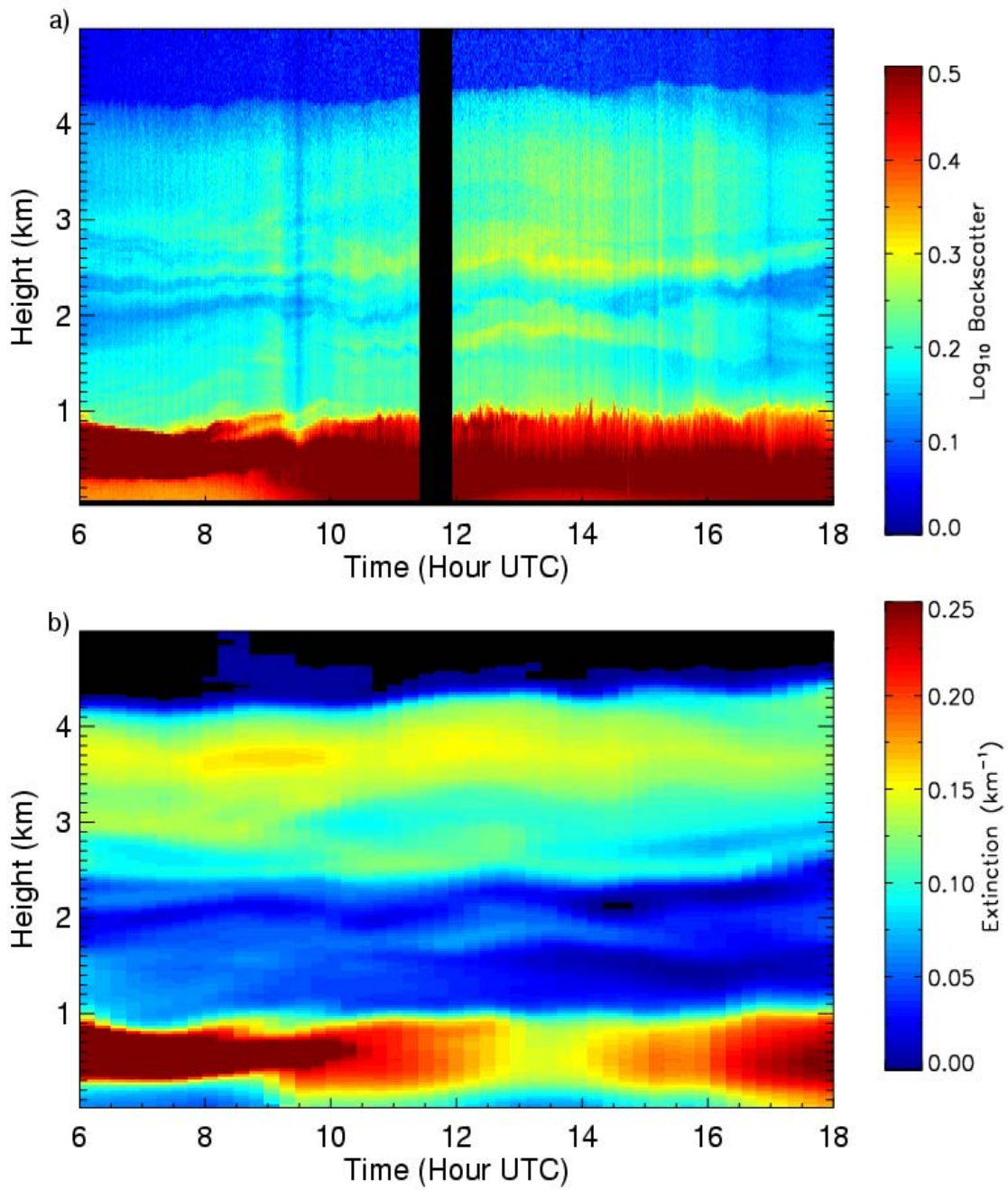


Figure 6. a) MPL corrected backscatter (relative units) and b) MPL-derived extinction profile for Jan 21 case study. Missing backscatter data near 12 UTC is due to closure of the MPL shutter to protect the optics; extinction profiles are interpolated over this period.

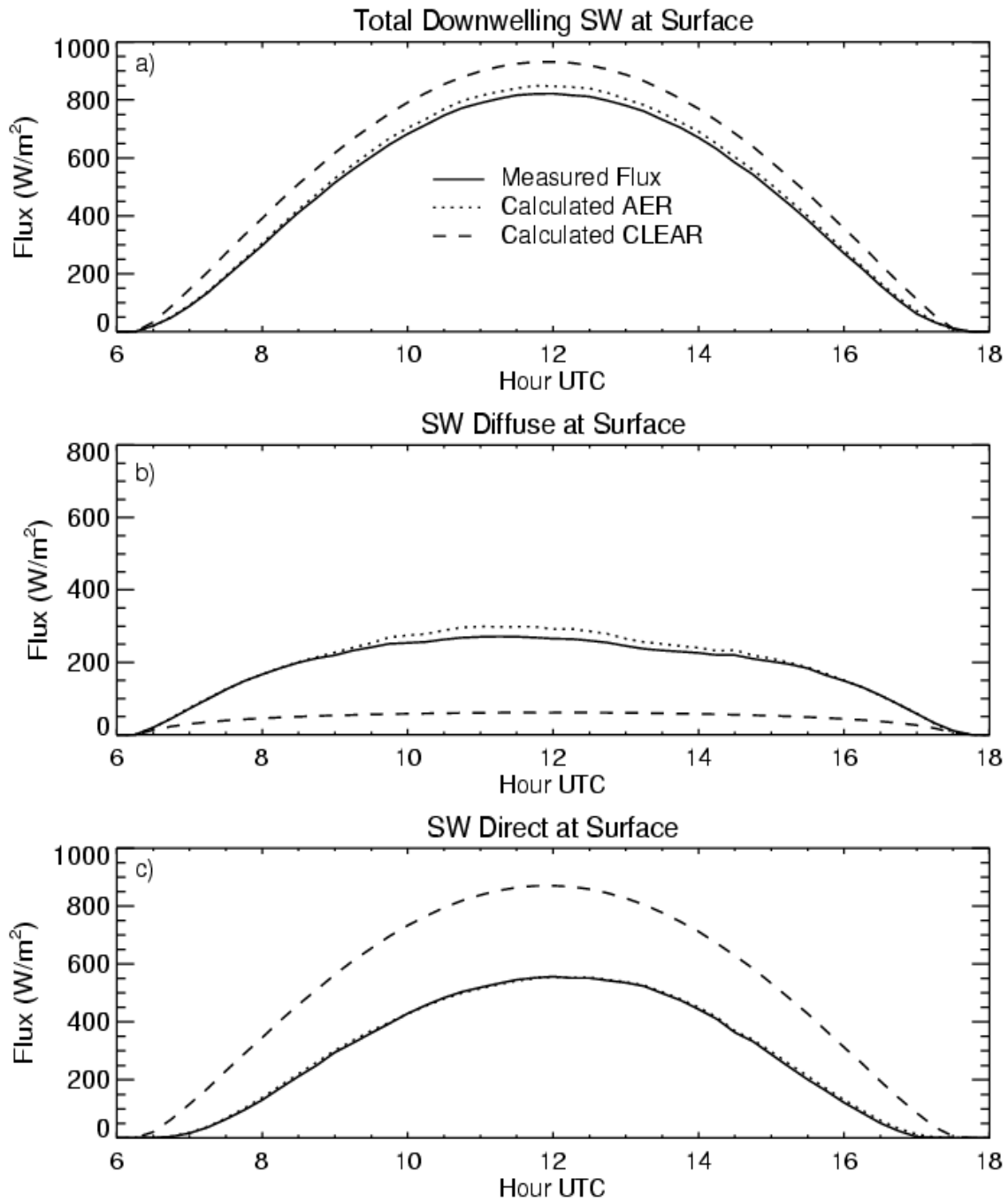


Figure 7. Observed and calculated a) shortwave total, b) diffuse, and c) direct fluxes at the surface for the Jan 21 case study. AER calculations include aerosol, but no clouds. CLEAR calculations use same atmospheric state inputs but have no aerosol.

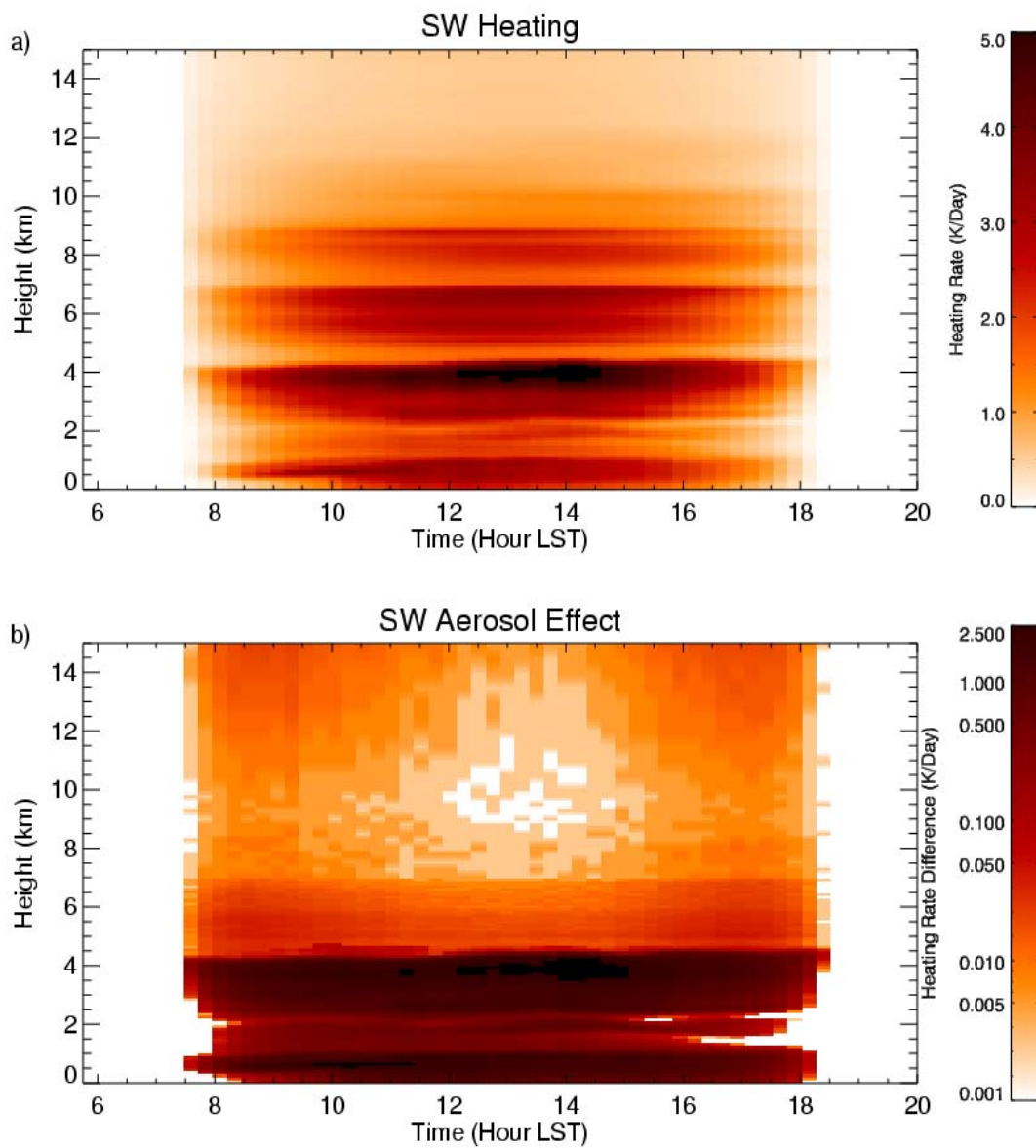


Figure 8. a) Calculated shortwave heating rate profile for Jan 21 case study. b) Aerosol effect on shortwave heating profile, defined as AER-CLEAR. Note log scale in lower panel.

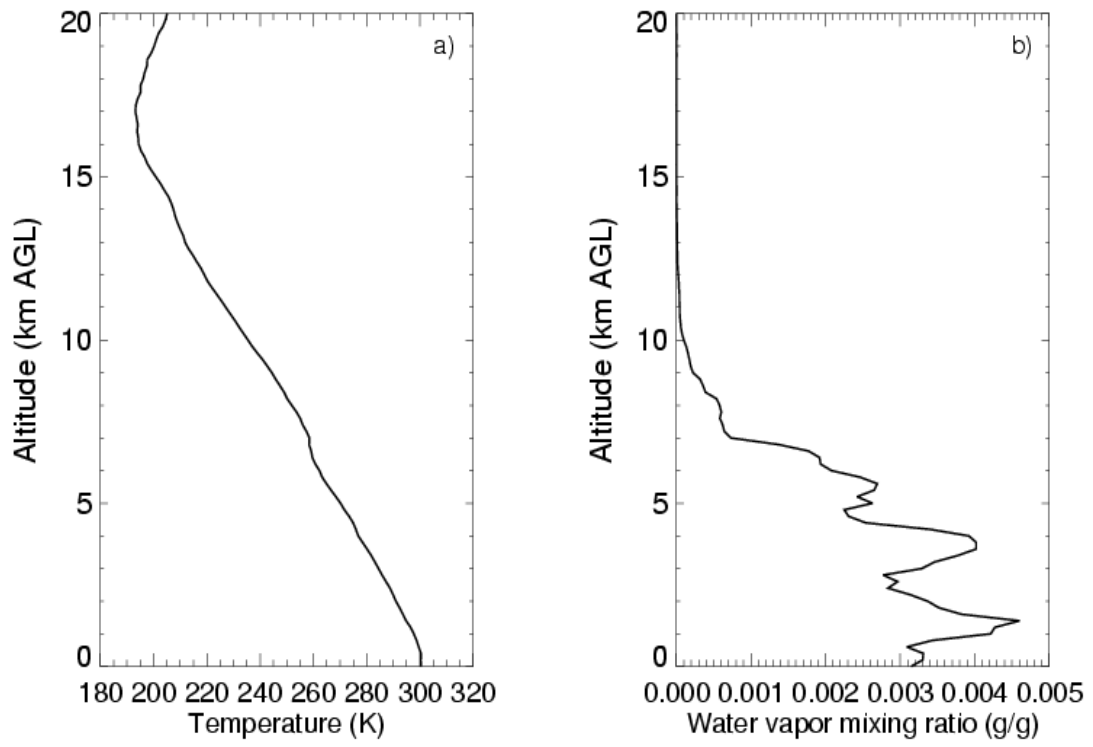


Figure 9. Average a) temperature and b) water vapor mixing ratio profiles derived from radiosonde data from Jan 21, 2006.

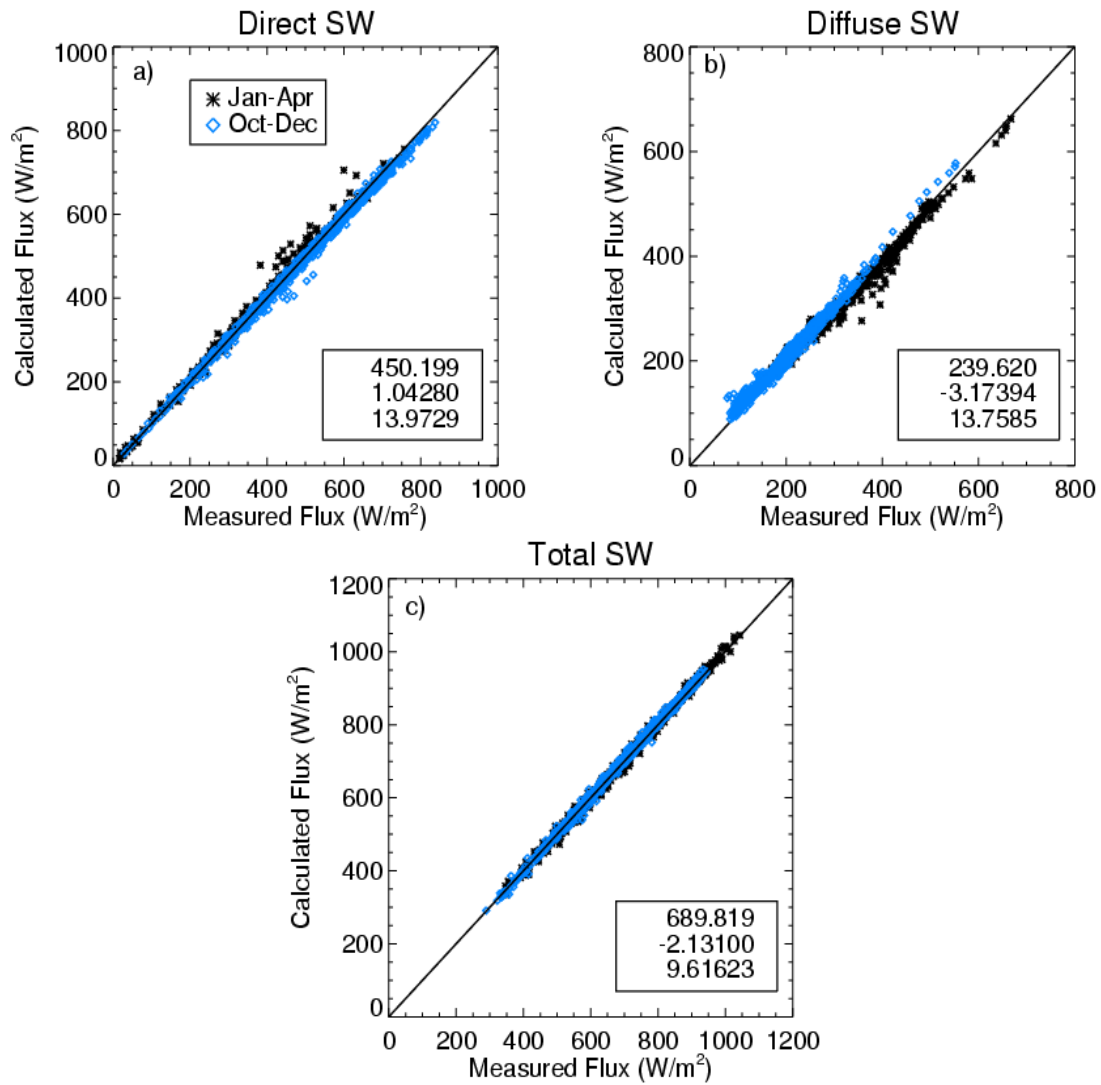


Figure 10. Comparison of calculated and measured a) direct, b) diffuse, and c) total downwelling shortwave fluxes at the surface for all non-cloudy 15 minute periods. Values given in each figure are mean observed flux, mean flux difference (AER-OBS), and RMS flux difference, respectively.

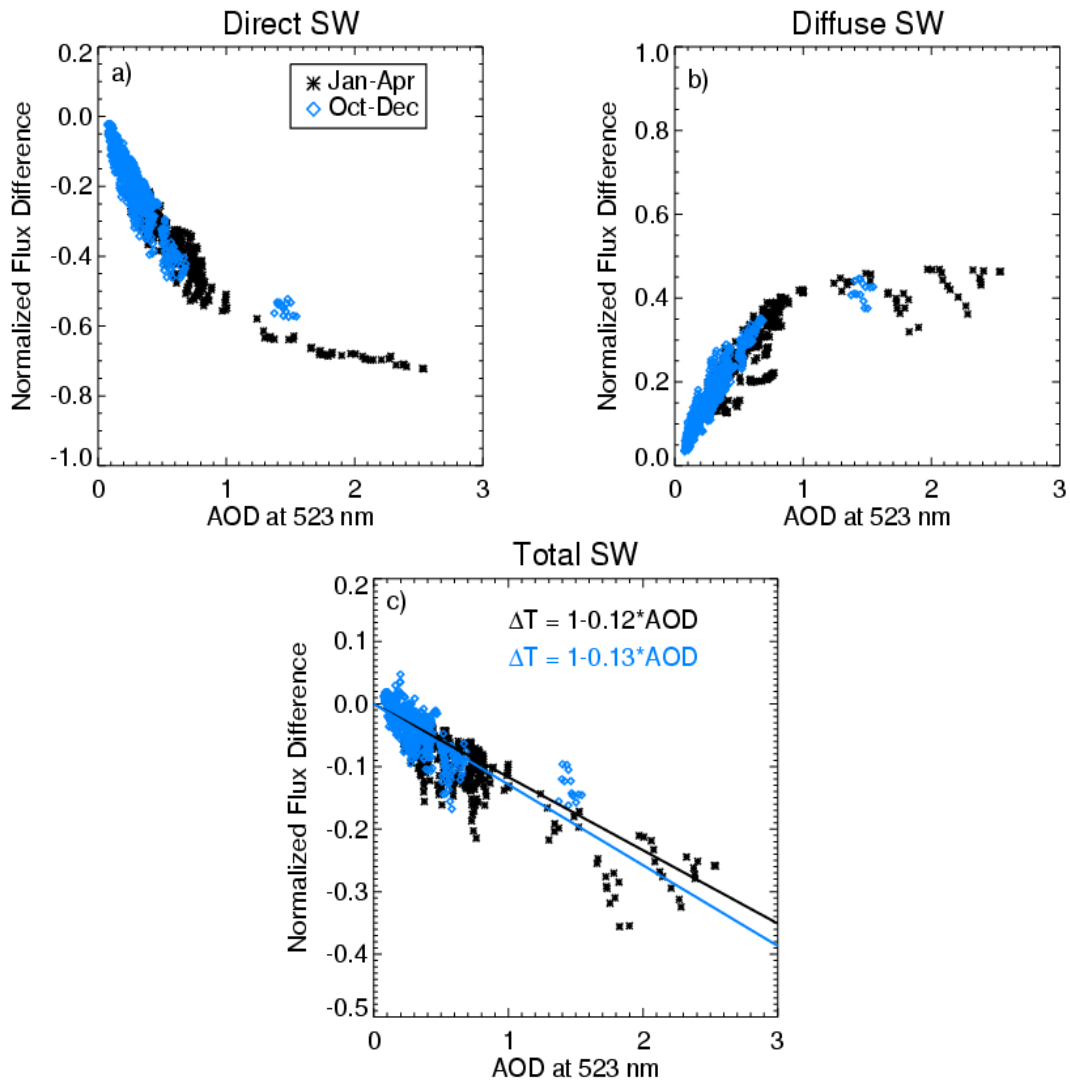


Figure 11. Normalized radiative effect of aerosols on downwelling SW at the surface for non-cloudy periods for a) direct SW, b) diffuse SW, and c) total SW. Normalized flux difference is calculated as the observed downwelling flux at the surface (OBS) minus the calculated downwelling flux at the surface (CLEAR) divided by incoming SW flux at the top of the atmosphere. Linear fit lines are described in the text.

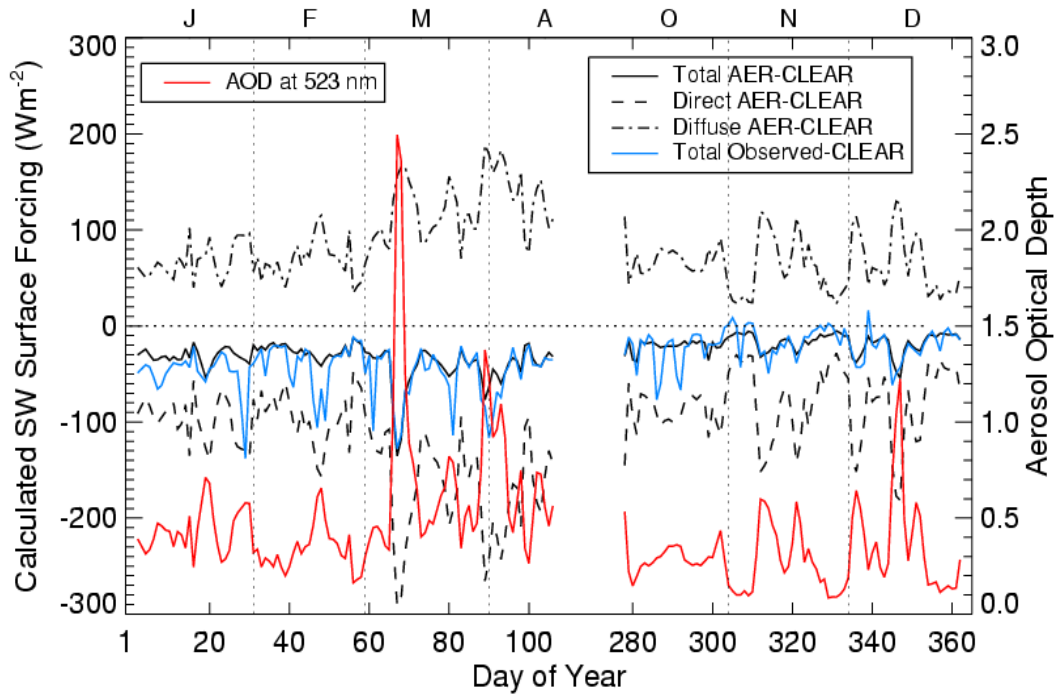


Figure 12. Time series of daily-averaged aerosol SW total (solid), direct (dashed) and diffuse (dashed-dotted) radiative forcing at the surface. Also included on the plot is the estimated daily-averaged aerosol + cloud total SW radiative forcing (blue) and the daily-averaged AOD (red). Note the discontinuity in the time axis.

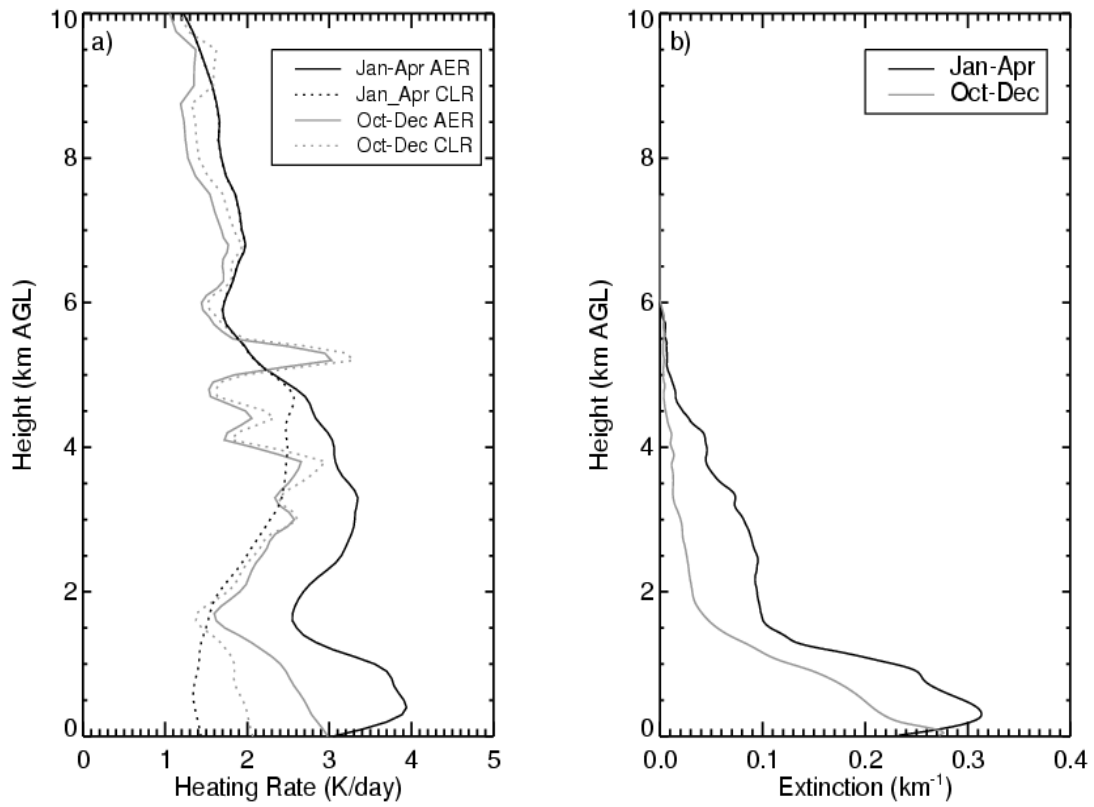


Figure 13. Average a) cloud-screened heating rate and b) extinction profile at 13:00 local time for Jan-Apr and Oct-Dec dry period